THERMOELECTRIC PROPERTIES OF QUANTUM DOTS AND OTHER

LOW-DIMENSIONAL SYSTEMS

by

NATTHAPON NAKPATHOMKUN

A DISSERTATION

Presented to the Department of Physics
and the Graduate School of the University of Oregon
in partial fulfillment of the requirements
for the degree of
Doctor of Philosophy

December 2010

"Thermoelectric Properties of Quantum Dots and Other Low-Dimensional Systems,"
a dissertation prepared by Natthapon Nakpathomkun in partial fulfillment of the
requirements for the Doctor of Philosophy degree in the Department of Physics. This
dissertation has been approved and accepted by:

_____

Dr. Richard Taylor, Chair of the Examining Committee

_____

Date

Committee in charge: Dr. Richard Taylor, Chair
                        Dr. Heiner Linke, Research Advisor
                        Dr. Dietrich Belitz
                        Dr. David Johnson
                        Dr. David Strom

Accepted by:

_____

Dean of the Graduate School

An Abstract of the Dissertation of

Natthapon Nakpathomkun   for the degree of   Doctor of Philosophy

in the Department of Physics   to be taken   December 2010

Title: THERMOELECTRIC PROPERTIES OF QUANTUM DOTS AND

OTHER LOW-DIMENSIONAL SYSTEMS

Approved: _____

Dr. Heiner Linke

Quantum dots are systems in which all three spatial sizes are comparable to the Fermi wavelength. The strong confinement leads to a discrete energy spectrum. A goal of thermoelectric research is to find a system with a high thermoelectric figure of merit, which is related to the efficiency of solid-state heat engines. The delta-like density of states of quantum dots has been predicted to boost this figure of merit. This dissertation addresses some thermoelectric properties relevant to the thermal-to-electric energy conversion using InAs/InP quantum dots embedded in nanowires.

In thermoelectric experiments, a temperature difference must be established and its value needs to be determined. A novel technique for measuring electron temperature across the dot is presented.

A strong nonlinearity of the thermocurrent as a function of temperature difference is observed at a small ratio of temperature gradient and cryostat temperature. At large heating currents, a sign reversal is observed. Numerical calculations explore the contribution of the energy dependence of the transmission function to this effect.

Depending on the relative contributions from sequential tunneling and co-tunneling, thermovoltages of quantum dots generally have one of two different lineshapes: a sawtooth shape or a shape similar to the derivative of the conductance peak. Here a simple picture is presented that shows that thermovoltage lineshape is accurately predicted from the energy level spacing inside the dot and the width of the transmission function.

An important figure of merit of all heat engines is the efficiency at maximum power. Here the thermoelectric efficiency at maximum power of quantum dots is numerically compared to that of two other low-dimensional systems: an ideal one-dimensional conductor (1D) and a thermionic power generator (TI). The numerical calculations show that either 1D or TI systems can produce the highest maximum power depending on the operating temperature, the effective mass of the electron, and the effective area of the TI system. In spite of this, 1D systems yield the highest efficiency at maximum power.

CURRICULUM VITAE

NAME OF AUTHOR: Natthapon Nakpathomkun

GRADUATE AND UNDERGRADUATE SCHOOLS ATTENDED:

> University of Oregon, Eugene, Oregon
> Chulalongkorn University, Bangkok, Thailand
> King Mongkut's Institute of Technology Thonburi, Bangkok, Thailand

DEGREES AWARDED:

> Doctor of Philosophy in Physics, 2010, University of Oregon
> Master of Science in Physics, 2002, Chulalongkorn University
> Bachelor of Science in Physics, 1996, King Monkut's Institute of
> Technology Thouburi

AREAS OF SPECIAL INTEREST:

> Thermoelectric Effects in Low-Dimensional Systems
>
> Mesoscopic Electron Transport

PROFESSIONAL EXPERIENCE:

> Graduate Research Assistant,
> University of Oregon, 2006 – 2007
> Graduate Teaching Fellow,
> University of Oregon, 2005 – 2006

GRANTS, AWARDS AND HONORS:

Royal Thai Government Scholarship 2005-2010

PUBLICATIONS:

Natthapon Nakpathomkun, Hongqi Q. Xu, and Heiner Linke, "Thermoelectric efficiency at maximum power in low-dimensional systems," manuscript submitted to Phys. Rev. B (e-print arXiv:10 10.1375)

E. A. Hoffmann, H. A. Nilsson, J. E. Matthews, N. Nakpathomkun, A. I. Persson, L. Samuelson, and H. Linke, "Measuring Temperature Gradients over Nanometer Length Scales," Nano Letters **9**, 779, (2009).

E. A. Hoffmann, N. Nakpathomkun, A. I. Persson, H. A. Nilsson, L. Samuelson, and H. Linke, "Determining a temperature differential across a quantum dot," Physica E **40**, 1605, (2008).

E. A. Hoffmann, N. Nakpathomkun, A. I. Persson, H. Linke, H. A. Nilsson, and L. Samuelson, "Quantum-dot thermometry," Appl. Phys. Lett. **91**, 252114, (2007).

ACKNOWLEDGEMENTS

TABLE OF CONTENTS

LIST OF FIGURES

CHAPTER I

INTRODUCTION

Nanostructured Thermoelectric Devices

Advanced semiconductor fabrication techniques have brought us a new venue to explore some unusual effects of quantum physics in mesoscopic devices. One of the new branches of research is exploring how to create devices that can convert a temperature gradient into electrical energy. This is the subject of this chapter on nanostructured thermoelectric devices.

Thermoelectricity

In 1821, Thomas Johann Seebeck observed that when there is a temperature difference across a material, a corresponding voltage is created. The parameter which indicates the magnitude of this voltage is the Seebeck coefficient, S, also known as thermopower. The definition of thermopower is the ratio of the open-circuit voltage to the applied temperature difference,

$$S = \left(\frac{\Delta V}{\Delta T} \right) \bigg|_{I=0},$$
(I.1)

where ΔV and ΔT are the voltage and temperature difference across the material, respectively.

In metals, the Seebeck coefficient is small (on the order of μV/K). The most well known application of this effect is the thermocouple where the temperature is determined by measuring voltage difference between two dissimilar species of metal or metal alloy with known Seebeck coefficients. From Fig. 1.1, the Seebeck coefficient of the top and bottom materials are

$$S_{1,2} = \frac{V_0 - V_{1,2}}{\Delta T},$$

where V_0 is the voltage at the joint of dissimilar metal. The voltage difference $V_1 - V_2$ then becomes,

$$\Delta V = (S_2 - S_1)\Delta T$$

and hence $\Delta T = \Delta V/(S_2 - S_1)$. The unknown temperature can be deduced from the measured ΔV, the knowns S_1 and S_2, and the known ambient temperature T.
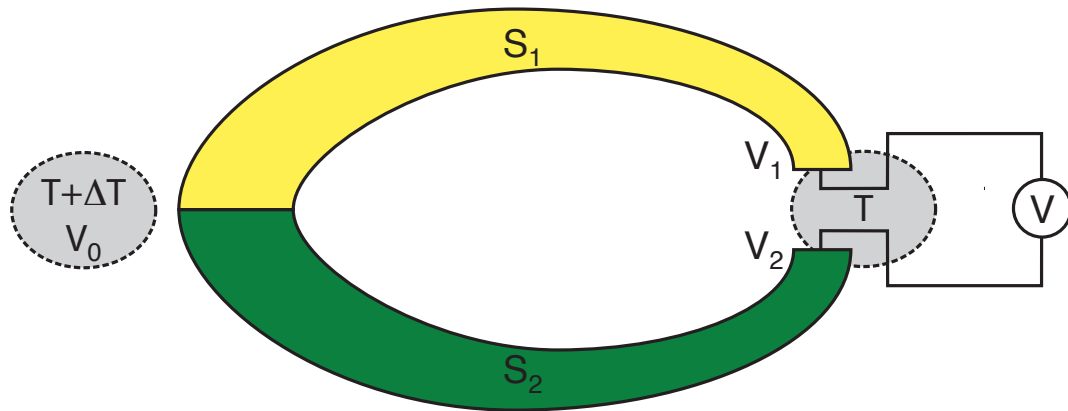
Figure 1.1. A thermocouple consists of two materials with known Seebeck coefficients, S_1 and S_2. The unknown temperature, $T + \Delta T$, can be determined from the voltage across the two ends, V, and the known temperature, T (see text for detail).

Other thermoelectric (TE) phenomena include the Thompson effect, in which heat is carried through a conductor by a charge current, owing to an applied temperature gradient; and the Peltier effect, in which an applied current passing through a junction of dissimilar material causes the junction to be warmer or cooler depending upon the direction of current flow. In other words, the Peltier effect is the reverse of the Seebeck effect. The ability of a material to convert a current to a temperature difference is quantified by the Peltier coefficient, Π. It is defined as the ratio of heat current to charge current under isothermal conditions,

$$\Pi = \left. \left(\frac{\dot{Q}}{I} \right) \right|_{\Delta T = 0}, \tag{I.2}$$

where I and $\dot{Q}$ are the charge and heat current through the material, respectively.

Thermoelectric phenomena involve the transport of charge and energy (in the form of heat). As electrons or holes flow through a conductor, they carry both charge and energy. In the linear response regime, the charge and heat current can be written as,

$$\begin{pmatrix} I \\ \dot{Q} \end{pmatrix} = \begin{pmatrix} G_V & G_T \\ M & L \end{pmatrix} \begin{pmatrix} \Delta V \\ \Delta T \end{pmatrix}, \tag{I.3}$$

where G_V, G_T, M, and L are thermoelectric transport coefficients. G_V is the electrical conductance. G_T and M are related through an Onsager relation, $M = -G_T T$. More familiar electrical and thermal coefficients can be deduced from Eq. I.3. For example, the definition of the electronic contribution to the total thermal conductance is given

by,

$$K = \left(\frac{\dot{Q}}{\Delta T} \right) \bigg|_{I=0}$$
$$= L + M \left(\frac{\Delta V}{\Delta T} \right) \bigg|_{I=0}. \quad (I.4)$$

The zero current condition leads to

$$S \equiv \Delta V / \Delta T = -G_T / G_V$$

and using the Onsager relation for M gives

$$K = L + M \left(-\frac{G_T}{G_V} \right)$$
$$= L - G_V T S^2. \quad (I.5)$$

Equation I.3 is more suitable for theorists. The experimentalist's version of Eq. I.3 can be written as

$$\begin{pmatrix} V \\ \dot{Q} \end{pmatrix} = \begin{pmatrix} R & S \\ \Pi & -K \end{pmatrix} \begin{pmatrix} I \\ \Delta T \end{pmatrix}, \quad (I.6)$$

where R is the electrical resistance ($R = 1/G$) and K is electronic thermal conductance. S is the Seebeck coefficient and Π is the Peltier coefficient as defined previously.

Thermoelectric Heat Engine

With the depleting fossil fuel resources and global warming, the world needs alternative energy resources. One strategy is to recycle some of the waste heat, such as heat from automobile exhaust, from industrial processes, or from photovoltaic energy conversion. Thermoelectric materials are candidates as direct thermal-to-electric energy converters. TE materials are a solid state thermoelectric heat engine.

This engine is different from the conventional fluid/gas based heat engine. In the conventional engine, such as the Joule/Brayton cycle and the Otto cycle, a working gas (or fluid) moves through cyclic thermodynamic steps as shown in Fig. 1.2. In thermoelectric engines, also called particle-exchange engines [1], the thermoelectric material electrically and thermally bridges particle reservoirs at different temperatures. As particles move from reservoir to reservoir, they absorb heat from a reservoir and then release heat to the other reservoir. The thermodynamic process is continuous and non-equilibrium. While the working gas of an ideal conventional heat engine is always in thermal equilibrium and has well-defined state variables such as temperature, the particles in a thermoelectric engine are lacking this property.

Figure 1.3 illustrates the TE modules for power generation and refrigeration. The module consists of n-type and p-type thermoelectric materials. In the power generating case, a temperature difference drives electrons (n-type) and holes (p-type) from the hot side to the cold side. As these particles move through thermoelectric materials, they perform work against an electric field, $\mathbf{E}$, that builds up because of charge imbalance.

The performance of thermoelectrics is typically quantified by the thermoelectric figure of merit, Z, which is defined as

$$Z = \frac{S^2 \sigma}{\kappa_e + \kappa_l},$$

(I.7)

where σ is the electric conductivity and $\kappa_{e,l}$ are the electrical and lattice thermal conductivities. Researchers also use the dimensionless figure of merit, ZT. The

(a) Cyclic Heat Engine
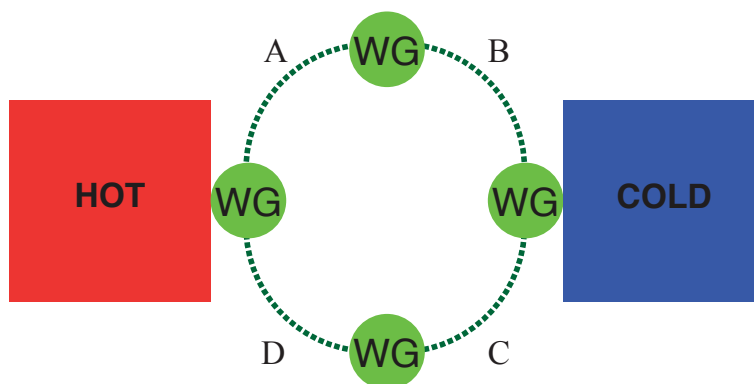
(b) Particle-Exchange Heat Engine
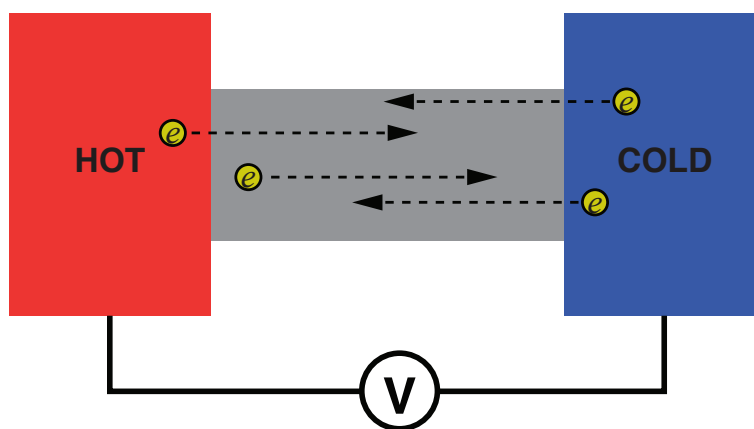
Figure 1.2. (a) Cyclic heat engine operates by cycling a working gas (WG) through thermodynamic steps, i.e. A-B-C-D-A. The cyclic heat engine produces work by absorbing heat from the hot bath, converting part of the heat into mechanical work, and releasing the rest to the cold bath. (b) A particle-exchange engine operates by a continuous flow of particles between hot and cold reservoirs. The particles carry charge and energy as they flow through the thermoelectric material. As they move along the material, they do work against the electrostatic potential created by charge imbalance.
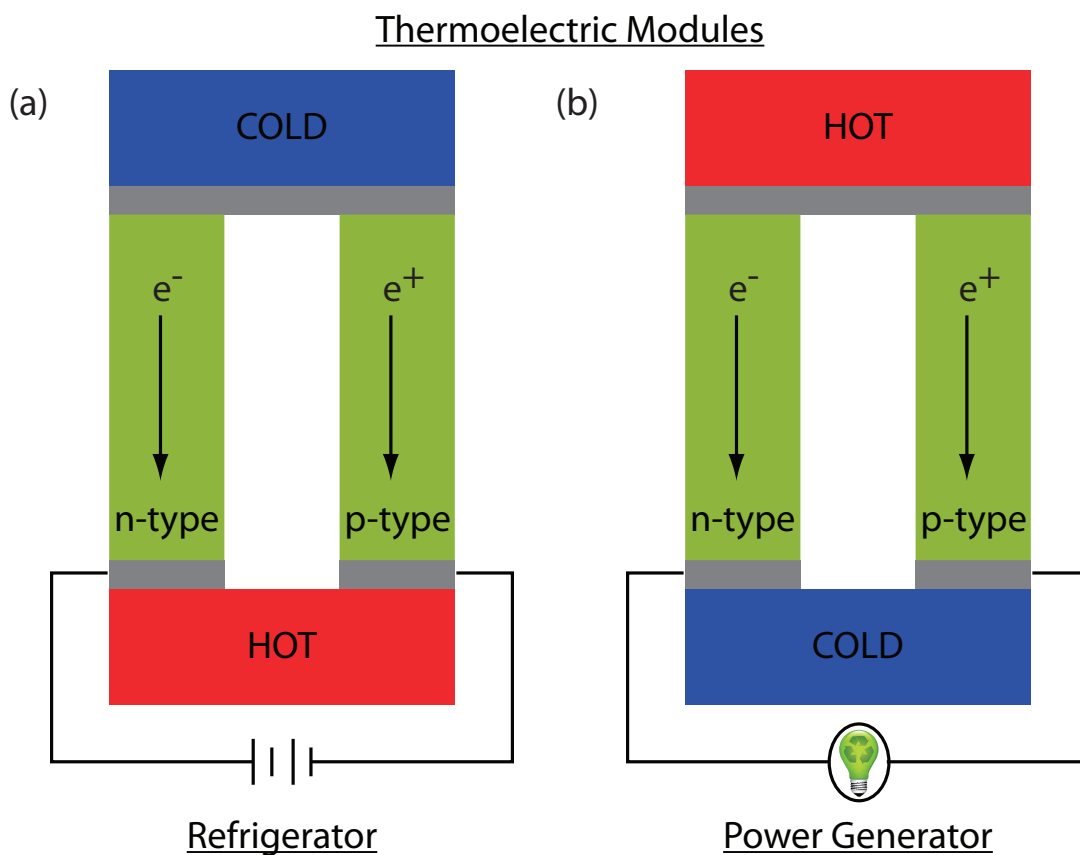
Figure 1.3. Schematic of a thermocouple. It consists of two conducting materials joined at the top by a metal (gray) to form a junction. (a) In the refrigeration mode, the applied voltage causes electrons (holes) to flow through an n-type (p-type) material. As a result, both carriers transfer heat away from the junction cooling the top portion. (b) In the power generating mode, carriers flow from the hot side to the cold side as a result of the applied temperature difference and as they move, they do work against electric field, **E**.

figure of merit is related to the efficiency (η) of the systems via

$$\begin{aligned}
\eta &= \frac{\Delta T}{T_H} \left(\frac{B-1}{B + T_C/T_H} \right) \\
&= \eta_C \left(\frac{B-1}{B + T_C/T_H} \right)
\end{aligned} \qquad (\text{I.8})$$

where $T_{H,C}$ is the electron temperature of the hot and the cold reservoirs, $\eta_C = \Delta T/T_H$

is the Carnot efficiency, and

$$B = 1 + \sqrt{ZT_{\text{av}}}$$

where $T_{\text{av}} = (T_H + T_C)/2$ is the average temperature.

Solid state heat engines have some advantages over conventional heat engines. These advantages include reliability, scalability, portability, and the absence of moving parts. Examples of such devices are portable coolers, car seat coolers/heaters, and power sources in deep space programs. However, the performance of thermoelectric nanostructured devices is inferior to conventional systems. The best ZT value available for commercial uses is about 1 which corresponds to roughly 10% of Carnot efficiency [2]. Though a ZT value of about 3.5 at 575 K has been reported [3], this technology is still in the research and development (R&D) phase, and some questions about the validity of these results exist. The lack of high-performance thermoelectrics is the reason these devices only exist in niche markets. In order to compete in mass market, thermoelectric devices need to have system ZT of at least 2 [2, 4–6].

Low-Dimensional Electron Systems

In bulk TE materials, thermoelectric parameters are not entirely independent from each other. For example, trying to increase the electrical conductance will unavoidably increase the thermal conductance, since particles carry both charge and energy (heat). Hence improvements using bulk TE material are limited. Low-dimensional systems, on the other hand, introduce a new variable of length scale which allows these parameters to be tuned quasi-independently. This can lead to ZT enhancement.

In the early 90s, the Dresselhaus group at MIT predicted that low-dimension electron systems such as Bi quantum wires or quantum wells can improve ZT compared to bulk Bi [7, 8]. This idea brought new attention from research communities. Since then, a variety of low-dimensional systems have been studied for their ability to compete with conventional engines. Examples of these systems include carbon nanotubes [9, 10], quantum dot superlattices [3, 11, 12], thin film semiconductors [13], and nanowires [14–16]. There are two strategies to boost ZT: one is the size quantization effect and the other is the use of interfaces to scatter phonons.

Size Quantization

Size quantization is a quantum effect in which energy states of the system change from continuous to discrete when a length of the system becomes comparable to the

Fermi wavelength. In the semiclassical picture, the energy of an electron is

$$E = \frac{\hbar^2(k_x^2 + k_y^2 + k_z^2)}{2m^*} \tag{I.9}$$

where m^* is the effective mass, assumed to be isotropic in all 3 directions. When the length along one of these directions becomes comparable to Fermi wavelength, the corresponding momentum is quantized. For example, if the length along the z-axis becomes comparable to the Fermi wavelength, then the total energy can be written as

$$E = \frac{\hbar^2(k_x^2 + k_y^2)}{2m^*} + E_{n_z}(z), \tag{I.10}$$

where E_{n_z} is the discrete energy level for the z direction. This is the energy of two-dimensional (2D) electron systems.

The density of states (DOS) is modulated as a result of this quantization (see Fig. 1.4). A sharp increase of the DOS near the Fermi energy could lead to substantial enhancement in the Seebeck coefficient, as explained as following. In the linear response regime, the thermoelectric coefficients in Eq. I.3 can be written as (using the Landauer formula, see chapter II)

$$G_V = -\frac{2e^2}{h} \int \frac{\partial f}{\partial E} \tau(E) dE$$

$$G_T = -\frac{2e^2}{h} \frac{k}{e} \int \left(\frac{E - \mu}{kT}\right) \frac{\partial f}{\partial E} \tau(E) dE \tag{I.11}$$

$$\frac{K}{T} = \frac{2e^2}{h} \left(\frac{k}{e}\right)^2 \int \left(\frac{E - \mu}{kT}\right)^2 \frac{\partial f}{\partial E} \tau(E) dE,$$

where the Fermi-Dirac distribution is defined as

$$f(E) = \frac{1}{1 + \exp(\xi)},$$

where

$$\xi = \frac{E - \mu}{kT},$$

and μ and k are an electrochemical potential and Boltzmann constant, respectively. All integrands depend on the Fermi window defined by $(-\partial f/\partial E)$. The density of states is closely related to τ. This means that if DOS increases rapidly within this window, these coefficients will also increase. The Seebeck coefficient, $S = -G_T/G_V$, and G_V of the low-dimensional systems get a boost from the modulated DOS compared to the gradually increasing DOS of the bulk system.

Phonon Heat Leak

From Eq. I.7, it is obvious that ZT can also be increased via the reduction of thermal conductivity. Heat leaks which reduce the efficiency of the engine consist of two parts: one is the charge carrier itself, quantified by the electronic heat conductivity κ_e and the other is the phonon (lattice), quantified by the phononic heat conductivity κ_l.

In metals, the electronic contribution κ_e is larger than the phonon contribution κ_l. In semiconductors, the opposite is true which means generally κ_l is larger than κ_e. Thus it is important to incorporate a way to reduce the phonon heat leak. This can be accomplished by utilizing many interfaces of low-dimensional systems. Because these interfaces in these systems can scatter phonons more efficiently than bulk systems, they reduce heat loss from the system [12, 13].
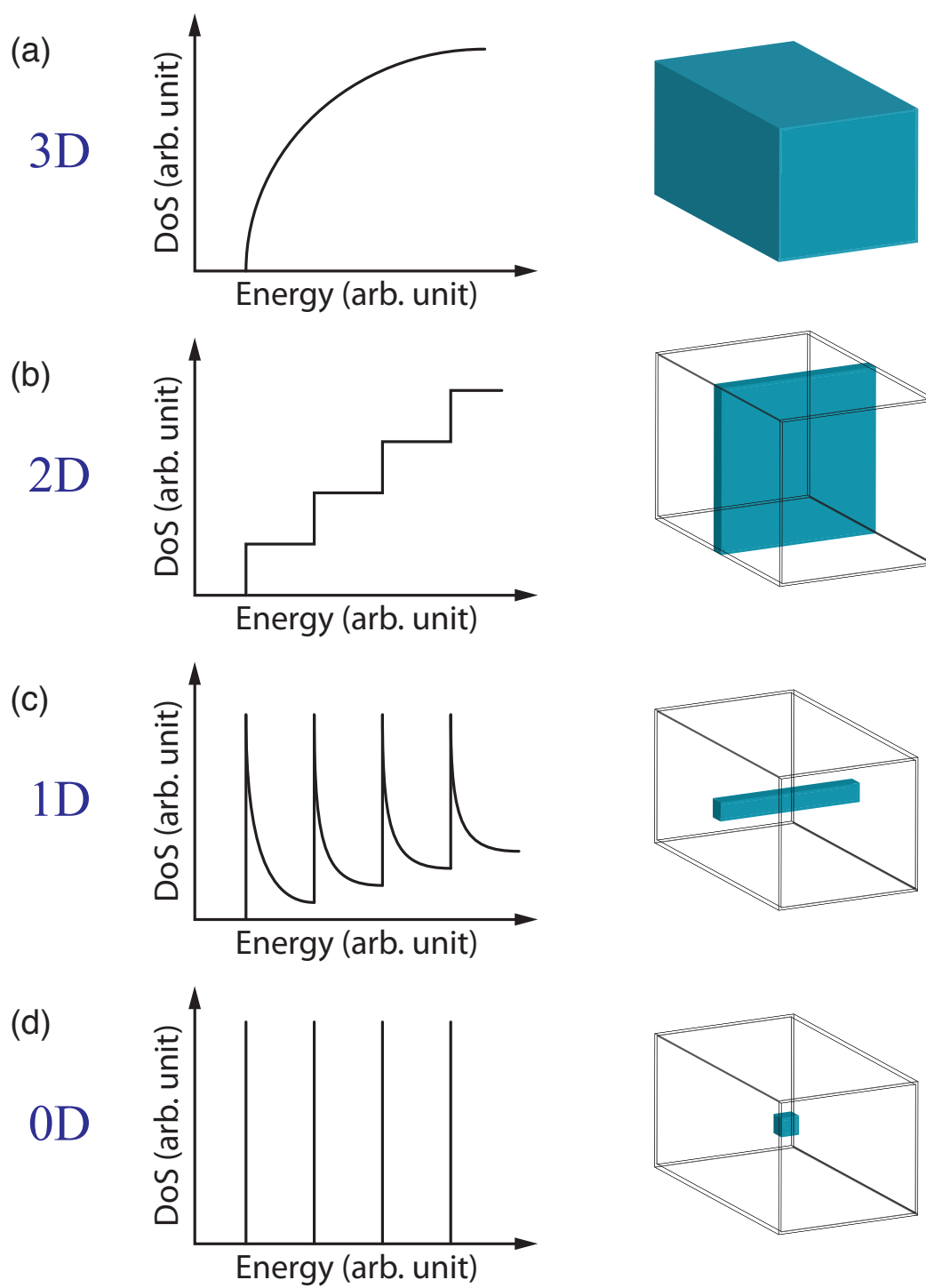
Figure 1.4. The density of states of each dimensional system. The bulk (3D) has a smooth DOS while the others have abrupt changes at each new energy state.

<center>Carnot Efficiency</center>

In 1996, Mahan and Sofo suggested that a system with a delta-like density of states could have the highest ZT [17]. It has been predicted that an energy filter with a very narrow energy range could be tuned to achieve reversible electron transport and electrons at this energy will flow without creating entropy [18, 19].

Carnot efficiency is achieved when there is no entropy creation results from the transport process. When an electron flows from the hot to the cold reservoir, the entropy associated with this process can be written as

$$\Delta \mathcal{S} = \frac{Q_H}{T_H} + \frac{Q_C}{T_C}. \tag{I.12}$$

where $\Delta \mathcal{S}$ is the entropy of the system, and $T_{C/H}$ are the temperatures of the hot and cold reservoirs. The heat carried out of the hot reservoir is $Q_H = -(E - \mu_H)$ while the heat added to the cold reservoir is $Q_C = (E - \mu_C)$. Reversibility is reached when electrons flow only at a specific energy:

$$E_0 = \frac{\mu_C T_H - \mu_H T_C}{T_H - T_C}. \tag{I.13}$$

This equation is obtained by inserting $Q_{H,C}$ into Eq. I.12 and equating this equation with zero. At this energy, E_0, the Fermi-Dirac distributions on both reservoirs are equal, $f_H(E_0) = f_C(E_0)$. The system reaches reversibility when there is no preferred direction of flow. A device with delta-like DOS, such as a quantum dot, can be used as an energy filter and can be tuned such that an energy level of the dot coincides with E_0. The resulting system then will behave as if at thermal equilibrium, and

energy conversion at Carnot efficiency (and at zero power) can take place. This is why a system with delta-like density of states could provide the highest efficiency.

Efficiency at Maximum Power

Quantum dots have been predicted to achieve an electronic efficiency near the Carnot limit [18]. However, as the system approaches this limit, the power generation decreases toward zero. This is because in the reversible limit there is no preferred direction of flow, so the net current (and thus the net power) is zero. In reality, the DOS of the quantum dot will have a finite width, which leads to electrons within some energy ranges near a resonant peak at E_0 (Eq. I.13) to flow and hence increase the power. Unfortunately, the efficiency of the quantum dot will then decrease. This is because some electrons are allowed to carry extra energy while contributing equally to the current and power. Also the transport of electrons at energies other than E_0 (see Eq. I.13) is an irreversible process and leads to entropy creation. Hence the efficiency becomes lower than the Carnot limit.

To utilize a quantum dot as a power generator, an equally important property would be the efficiency at maximum power, denoted by η_{maxP}. Curzon and Ahlborn [20] have shown that the efficiency at maximum power, obtained by optimizing the

Carnot cycle with respect to power instead of efficiency, is

$$\eta_{CA} = 1 - \sqrt{\left(\frac{T_C}{T_H}\right)}$$

$$= 1 - \sqrt{(1 - \eta_C)}$$

$$= \frac{\eta_C}{2} + \frac{\eta_C^2}{8} + \ldots \tag{I.14}$$

Recently it was shown that this limit is universal up to the second-order term [21–23]. This sets the upper limit of efficiency for any heat engine operating at maximum power.

Outlook

Electron transport in quantum dots has been extensively studied. Far less attention has been given to the thermoelectric properties. This dissertation aims to address some of the properties that affect the thermoelectric performance of a quantum dot. Quantum dots in this study are defined by InP double barriers embedded in InAs nanowires.

A quantum dot with its discrete energy spectrum operates as an energy filter in which only electrons with a particular energy matching the lowest unoccupied energy state of the dot can move into and out of the dot. QDs have a potential to operate as a high ZT heat engine with efficiency approaching the Carnot limit and be able to compete with conventional power generators or refrigerators. Thus, QDs are useful

to scientists and engineers for understanding the device properties that can affect thermoelectric performance of heat engines.

As mentioned in the previous section, it is not only efficiency and ZT that are relevant in determining thermoelectric performance but also the efficiency at maximum power. Here η_{maxP} of three low-dimensional systems will be numerically compared using the Landauer formalism. These systems are a quantum dot, a one-dimensional conductor such as a nanowire, and a thermionic power generator formed by a two-dimensional energy barrier.

CHAPTER II

THEORY OF A QUANTUM DOT

This chapter provides a review of the theoretic modeling used in this dissertation. First, the physics of the quantum dot is presented using the constant interaction model. Then theory of electron transport in a quantum dot using the Landauer formalism is presented. Finally, using this theory, theoretical derivations of thermoelectric quantities are presented.

The Physics of Quantum Dots

A quantum dot is a system in which all three spatial dimensions are defined such that these lengths are comparable to the Fermi wavelength of electrons. The confinement reveals the quantum nature of electrons in the dot and leads to discrete energy levels similar to those found in atoms, as shown in Fig. 2.1. Sometimes quantum dots are referred to as artificial atoms.

Another feature of quantum dots is charge quantization. When the dot is weakly coupled to the contacts, the number of electrons in the dot is an integer number. As current flows from source to drain, this number is fluctuating by one. Because of Coulomb repulsion, adding another electron requires extra energy and this energy can be large compare to kT. The discreteness of charge on the dot leads to Coulomb

blockade phenomenon where electron transport is forbidden if electrons from reservoirs do not have enough energy to compensate for Coulomb repulsion. The blockade will be lifted if one of the dot energy levels aligns with the electrochemical potential of either source or drain contacts. The result is the periodic fluctuation in conductance as a function of gate voltage.

Coulomb blockade has been successfully described by the constant interaction model. This section will briefly review the relevant physics of Coulomb blockade of quantum dots. For comprehensive reviews see [24, 25]. This model is based on two assumptions. First, Coulomb interaction between electrons in the dot and its environment (the source, drain, and gate contacts) can be parameterized by a single capacitance, $C = C_S + C_D + C_G$ (see Fig. 2.1(b)), which is independent of the number of electrons in the dot. The second assumption is that the single energy-level spectrum, $\{E_n\}$, is independent of these interactions and N. Now consider the total energy for N and $N - 1$ electrons in the dot:

$$U(N) = \frac{[-e(N - N_0) + \sum_i C_i V_i]^2}{2C} + \sum_{n=1}^{N} E_n$$

$$U(N - 1) = \frac{[-e(N - 1 - N_0) + \sum_i C_i V_i]^2}{2C} + \sum_{n=1}^{N-1} E_n.$$

where V_i is the voltage between the dot and the contact i, and $\sum_i$ means summation of all three electrodes. E_n is a single-electron quantum energy level for the n-th electron and N_0 is the number of electrons on the dot at zero gate voltage. In each equation, the first two terms are discrete and continuous electrostatic energy, respectively, while
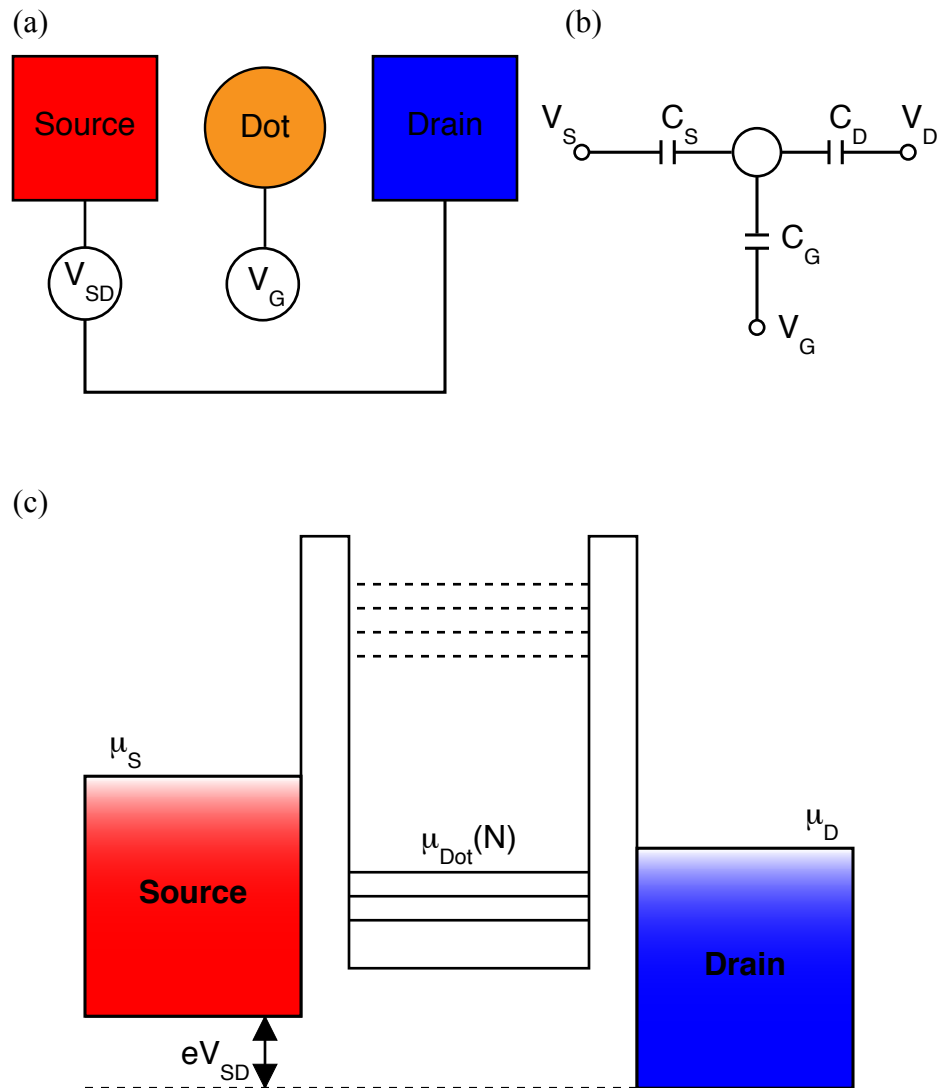
Figure 2.1. (a) A schematic represents the circuit of quantum dot. (b) The constant interaction model describes the total interaction of the dot with its environment by the capacitance, $C = C_S + C_D + C_G$. (c) Energy diagram of the circuit of the quantum dot and its leads. The solid lines are occupied resonant levels while the dashed lines are emptied levels. The highest occupied level is indicated by $\mu(N)$. The applied bias creates the chemical potential difference of the contacts, $V_{SD} = (\mu_S - \mu_D)/e$.

the last term is the energy level from size quantization. The electrochemical potential associated with N electrons on the quantum dot is defined as

$$\mu(N) = U(N) - U(N-1)$$

$$= \left(N - N_0 - \frac{1}{2}\right) E_C - \frac{E_C}{|e|}\left(\sum_i C_i V_i\right) + E_N, \tag{II.1}$$

where $E_C = e^2/C$ is the charging energy. The energy required for adding or removing an electron from the dot is

$$E_{\text{add}} = \mu(N+1) - \mu(N)$$

$$= \left[\left(N - N_0 + \frac{1}{2}\right) E_C + E_{N+1}\right] - \left[\left(N - N_0 - \frac{1}{2}\right) E_C - E_N\right]$$

$$= E_C + (E_{N+1} - E_N)$$

$$= E_C + \Delta E. \tag{II.2}$$

This equation indicates that the energy spectrum of the dot has two parts: the size-quantized energy and the charging energy. In the small dot where $\Delta E \gg E_C$, the energy level of the dot is dominated by the size quantization effect.

From Eq. II.1, μ is a function of gate voltage. When $\mu(V_G)$ is equal to E_{add}, then the Coulomb blockade is lifted. Sweeping of μ using V_G produces periodic oscillations of the conductance as a function of V_G. This provides a spectroscopic tool for energy characterization of the dot. Furthermore, one can measure the conductance as a function of V_{SD} and V_G (see figure 2.2). Using this data, one can quantify the linear relationship between V_G and μ. This relationship is useful for comparison between experimental data and theory because the experiment is controlled via V_G

but the energy diagram of the dot is described by μ. From Eq. II.1 and the condition $\mu(N, V_G) = \mu(N + 1, V_G + \Delta V_G)$, this relationship is

$$\Delta V_G = \frac{C}{eC_G}\left(\Delta E + \frac{e^2}{C}\right) = \frac{C}{eC_G}\Delta\mu. \tag{II.3}$$

This equation requires that the proportional constant, C_G/C, is known.

<u>Modeling: The Landauer Formalism</u>

In this dissertation, the main theoretical tool is the Landauer formalism. This approach is based on the idea that electron transport through a conductor is determined from the likelihood that a charge carrier can successfully transmit from one reservoir to the other [26].

Consider two electron reservoirs (contacts) bridged by a conductor whose length is smaller than the electron elastic scattering length. Electrons in each reservoir have a well-defined temperature and chemical potential. Let the left contact represent the hot side and denote temperature and chemical potential by T_H and μ_H, respectively. Correspondingly, let the right contact represent the cold side and denote temperature and chemical potential by T_C and μ_C, respectively. The applied bias is defined as $V_{SD} = (\mu_C - \mu_H)/e$. Electrons in the hot and cold reservoirs can then be described by the Fermi-Dirac distributions:

$$f_{H/C}(E, \mu_{H/C}, T_{H/C}) = \left[1 + \exp\left(\frac{E - \mu_{H/C}}{kT_{H/C}}\right)\right]^{-1}. \tag{II.4}$$

In the ballistic regime, the scattering occurs at the interface between the conductor
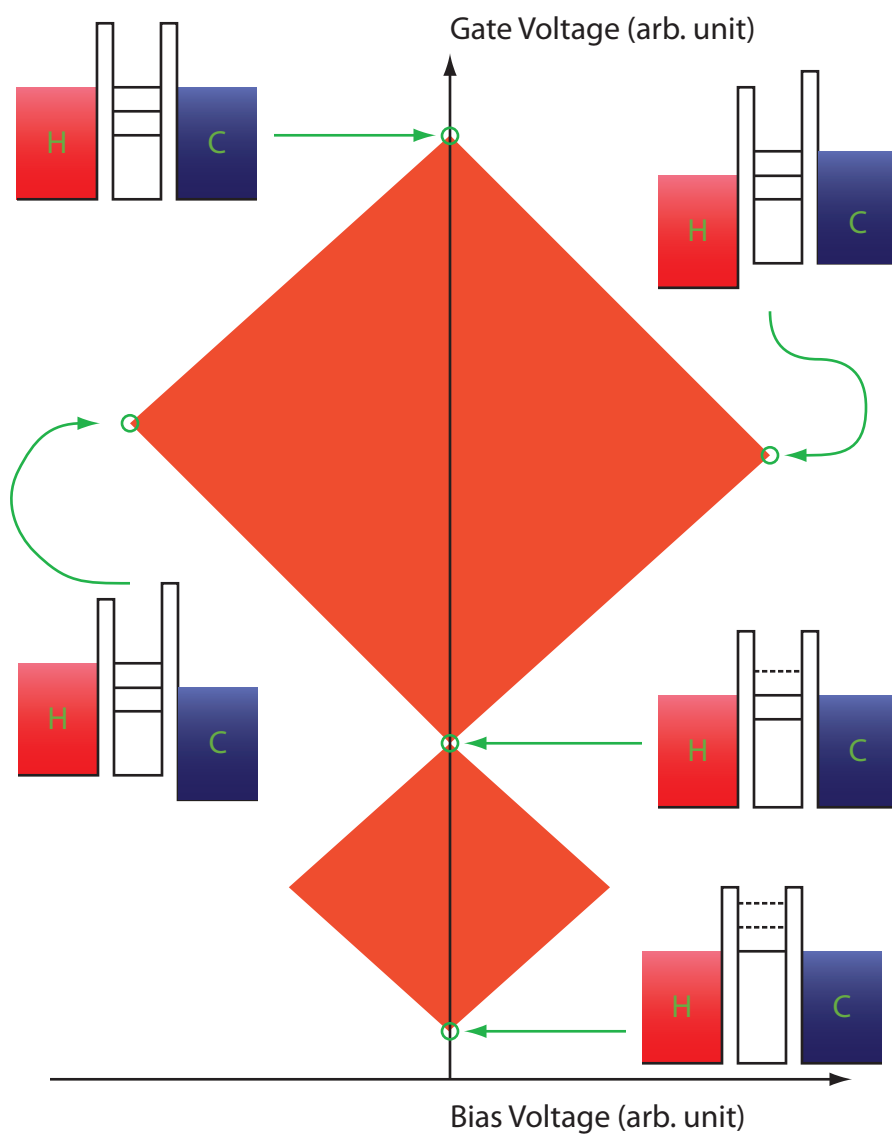
Figure 2.2. Schematic energy diagram of the quantum dot in various positions of a Coulomb blockade diamond (stability diagram).
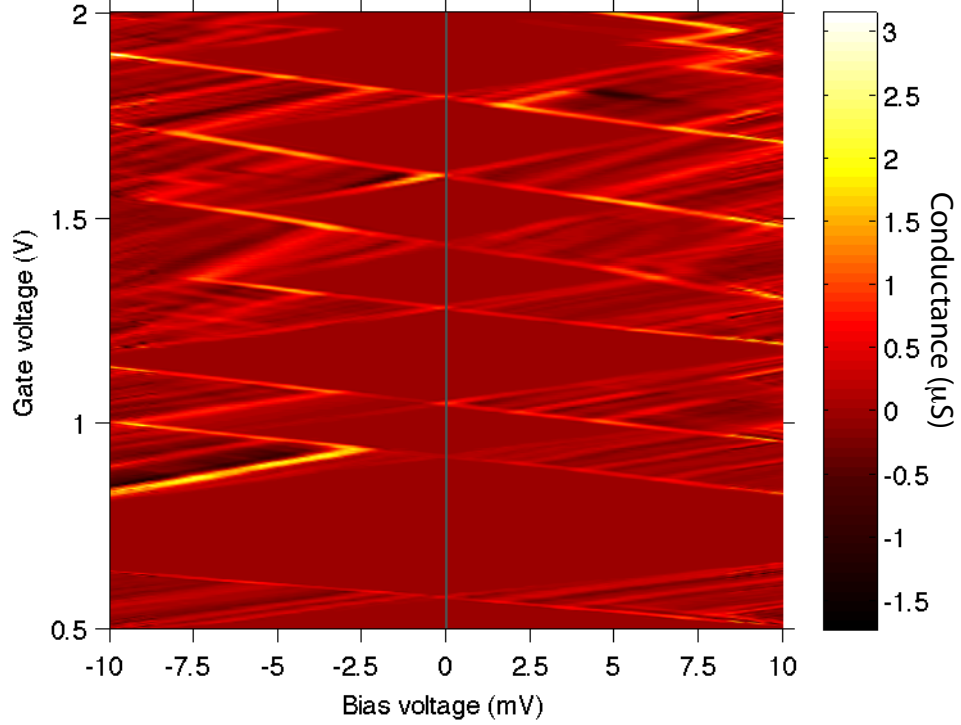
Figure 2.3. Coulomb blockade diamond of differential conductance as a function of bias and gate voltages measured at $T = 550$ mK.

and reservoirs. From quantum mechanics, this scattering can be expressed in terms of an energy-dependent transmission function, $\tau(E)$.

The total momentum of a single electron in a one-dimensional conductor is composed of the quantized momentum in the transverse directions and the (non quantized) momentum of a single electron in the longitudinal direction (parallel to the z-axis). Assuming a parabolic dispersion relation, $E = p^2/2m = (\hbar k)^2/2m$, the total energy can be written as:

$$E = \epsilon_N(x, y) + \frac{(\hbar k_z)^2}{2m}, \qquad \text{(II.5)}$$

where $\epsilon_N(x, y)$ is the quantized energy in the x-y plane and k_z is the wave vector

in the z-axis. For a single transverse mode with cut-off energy ϵ_N, current from the

hot(left) to the cold(right) reservoirs is

$$i^+ = \frac{e}{L} \sum_{+k} v f(E(+k)) = \frac{e}{L} \sum_{+k} \frac{1}{h} \frac{\partial E}{\partial k} f(E(+k)). \tag{II.6}$$

Replacing the summation by an integral,

$$\sum_{+k} \rightarrow \frac{L}{2\pi} \int dk, \tag{II.7}$$

and changing variables from momentum to energy, gives

$$i^+ = \frac{2e}{h} \int_{\epsilon_N}^{\infty} f^+(E) dE. \tag{II.8}$$

The factor of 2 accounts for the spin degeneracy. In the same way, the current from

cold(right) to hot(left) sides is

$$i^- = \frac{2e}{h} \int_{\epsilon_N}^{\infty} f^-(E) dE. \tag{II.9}$$

The net current is

$$i = \frac{2e}{h} \int_{\epsilon_N}^{\infty} [f^+(E) - f^-(E)] dE. \tag{II.10}$$

In general, the current also depends on the chance that electrons can flow from one

reservoir to the other. Thus the net current can be written as,

$$i = \frac{2e}{h} \int_{\epsilon_N}^{\infty} [f^+(E) - f^-(E)] \tau_{1D}(E) dE, \tag{II.11}$$

where $\tau_{1D}(E)$ is the energy-dependent transmission probability that electrons can

transmit through the 1D channel. Equation II.11 is the Landauer formula for a two-

terminal conductor. This equation is also valid for a quantum dot and one only

has to replace $\tau_{1D}(E)$ with $\tau_{QD}(E)$. For the Lorentzian approximation [27, 28], the transmission of a quantum dot with only one transmission resonance within many kT of the chemical potential can be written as

$$\tau_{QD}(E) = \frac{(\Gamma/2)^2}{(E - E_0)^2 + (\Gamma/2)^2}, \tag{II.12}$$

where E_0 is the energy of the resonant level and Γ is the full width at half maximum of the resonance.

Derivation of Thermoelectric Quantities

Numerical calculations of thermoelectric quantities in this dissertation are done using Matlab based on the equations derived in this section. These include current, thermovoltage, power, efficiency, electrical and thermal conductance, and the ZT figure of merit.

Current

Consider a quantum dot connected to the hot and cold reservoirs. In general, both electrochemical potentials (μ_H, μ_C) and temperatures (T_H, T_C) of each reservoir can have different values. From the two-terminal Landauer formula (Eq. II.11), one can calculate the current as a function of $\mu_{H/C}$ and $T_{H/C}$ as

$$I(V, \mu) = -\frac{2e}{h} \int [f_H(E, \mu_H, T_H) - f_C(E, \mu_C, T_C)]\tau(E)dE. \tag{II.13}$$

Thermovoltage and Thermopower

By definition, the thermovoltage, denoted V_{th}, is the voltage created by a temperature difference, $\Delta T = T_H - T_C$, under the condition of zero net current. This is the open-circuit condition. Numerically, $V_{th} = (\mu_H - \mu_C)/e$ can be calculated via Eq. II.13 by searching for the μ_H and μ_C which result in $I = 0$. Such values of $\mu_H - \mu_C$ are not uniquely constrained. However, unique values of $\mu_{H/C}$ can be found by assuming that the voltage drops equally across each quantum dot barrier. Therefore, $\mu_{H/C} = \mu \pm eV_{th}/2$, where μ is the average chemical potential and is controlled externally by the gate voltage, V_G. The accuracy of V_{th} will depend on the number of V data points used in the search. Normally the numerical calculation does not always yield the exact zero. In the search for $I = 0$, one has to pick V that gives the current value closest to zero. It can take quite some time to obtain V_{th} if one chooses too small of a step size.

One can also calculate V_{th} from an approximated closed-form equation. Under the linear response approximation, $\Delta E, k\Delta T \ll kT$, where ΔE denotes the energy spacing of conducting material, the Fermi function of the hot and the cold contacts can be expanded around the equilibrium value (average T and μ). This gives $f_{H/C}$ as

$$f_{C,H} \approx f_0 \pm \frac{\partial f_0}{\partial E} \left[\left(\mu \pm \frac{V_{th}}{2} \right) - \left(\frac{E - \mu}{T} \right) (T - T_{C,H}) \right]$$

where f_0 is the Fermi function at equilibrium conditions ($\mu_H = \mu_C$ and $T_H = T_C$).

Put these into Eq. II.13

$$I(V, \mu) = -\frac{2e}{h} \int \frac{\partial f_0}{\partial E} \left[-eV_{th} - \left(\frac{E - \mu}{T} \right) \Delta T \right] \tau(E) dE = 0. \qquad \text{(II.14)}$$

Solving for V_{th} gives

$$V_{th} = -\frac{\Delta T}{eT} \frac{\int dE (E - \mu) \left(\frac{\partial f_0}{\partial E} \right) \tau(E)}{\int dE \left(\frac{\partial f_0}{\partial E} \right) \tau(E)}. \qquad \text{(II.15)}$$

Calculations performed using Eq. II.15 can be done in a shorter time than the numerical search method described above. But Eq. II.15 is only valid when $k\Delta T$ and eV_{th} are small compared to kT. Regardless of the method used to find V_{th}, one can easily obtain thermopower, S, directly from its definition, $S = -V_{th}/\Delta T$.

Heat Flux, Power, and Efficiency

When an electron moves through a channel, it carries both charge and energy. The heat removed from the hot reservoir by an electron that leaves the reservoir at energy E is $Q_H = (E - \mu_H)$. The rate at which heat leaves the reservoir per unit time is the heat flux out of the hot reservoir. By replacing electric charge with Q_H in Eq. II.6 and running through the derivation again, the heat flux, $\dot{Q}_H$ is obtained. The result of this is

$$\dot{Q}_H = (E - \mu_H) n \nu$$
$$= \frac{2}{h} \int dE (E - \mu_H) \tau(E) (f_H - f_C). \qquad \text{(II.16)}$$

Power is easily calculated from the definition of electric power: $P = IV$. Since I is a function of μ and V, then power is also a function of μ and V. In this calculation,

the power generated (thermally) by the device has a negative value, while power generated by an applied external voltage has a positive value. Therefore, when we present our modeling results, we will graph only negative power values and ignore all positive values (not included in the figures) so that they do not obscure features of the power generated by the dot.

The efficiency of a heat engine is the ratio of power output to heat flux, that is,

$$\eta = \frac{\text{Power (Energy output/time)}}{\text{Heat Flux (Energy input/time)}} = \frac{P}{\dot{Q}_H} \tag{II.17}$$

The thermoelectric efficiency describe in this dissertation will refer to efficiency as a heat engine.

Electrical and Thermal Conductances and ZT

Differential conductance (G) determines how easily electric charges can move in a conductor when a small bias is applied with a uniform temperature. The equation for G is

$$G = \frac{dI}{dV}\bigg|_{\Delta T = 0} = -\frac{2e}{h} \int dE \frac{\partial f}{\partial V} \tau(E). \tag{II.18}$$

For thermal conductance, only the electron contribution will be considered here. The electronic thermal conductance indicates how readily electrons carry heat through a conductor in the presence of a thermal gradient and in absence of an electrical current. It is defined as

$$K_e = \frac{\dot{Q}_H}{\Delta T}\bigg|_{I=0}. \tag{II.19}$$

To calculate the electronic ZT, one must calculate all three parameters in Eqs. II.15, II.18, and II.19 (thermopower, electric and thermal conductance) and then insert them into Eq. I.7.

CHAPTER III

EXPERIMENTAL METHODS

Device Fabrication

Nanostructure devices can be made by top-down or bottom-up approaches. In the top-down approach, portions of materials are removed by semiconductor techniques such as etching. In the bottom-up approach, the device is built up from smaller constituents using techniques such as molecular beam epitaxy (MBE) where molecules of growth species diffuse around and form desired structures.

InAs/InP heterostructure nanowires can be used as quantum dots [29]. InAs nanowires provide the lateral confinement while the dots are defined by InP barriers. Nanowire growth can be explained by the vapor-liquid-solid (VLS) mechanism which was first proposed by Wagner and Ellis [30]. In essence, a small metal particle, which provides a preferred site for the wire growth, is deposited on the substrate. Then the substrate is heated. When the system reaches an eutectic point, the particle and substrate form a liquid droplet. Then vaporized growth material is introduced into the liquid alloy. Once the eutectic alloy becomes supersaturated, the growth commences. The wire grows by precipitation of the growth species at the liquid-solid

interface. The wire continues to rise underneath the liquid droplet as long as the vapor growth species are steadily supplied.

InAs/InP Heterostructure Nanowires

The quantum dots used in our experiments were made by our colleagues at Lund University. III-V heterostructure nanowires were grown using chemical beam epitaxy (CBE) [31–34]. This approach differs from the VLS mechanism in that there is no liquid phase. In addition, the seed particle is in a solid phase instead of liquid during the growth [35, 36].

The procedure used at Lund to grow InAs/InP heterostructure nanowires is as follows [33, 34, 37, 38]: First size-selected Au seed particles are deposited onto InAs <111>B crystalline substrate, and then the substrate is transferred to the CBE vacuum chamber and heated. Then group III and V species are injected through separated lines. Because of its long diffusion length, the group III source (In) can reach seed particles by diffusion along the substrate and up the wire side walls or by direct impingement. For group V sources (As and P), the diffusion length is small, and only those source particles which directly impinge on the seed particle will contribute to the nanowire growth. Heterostructure nanowires are achieved by alternating between source species during the growth process. Figure 3.1 shows the summary of this procedure.
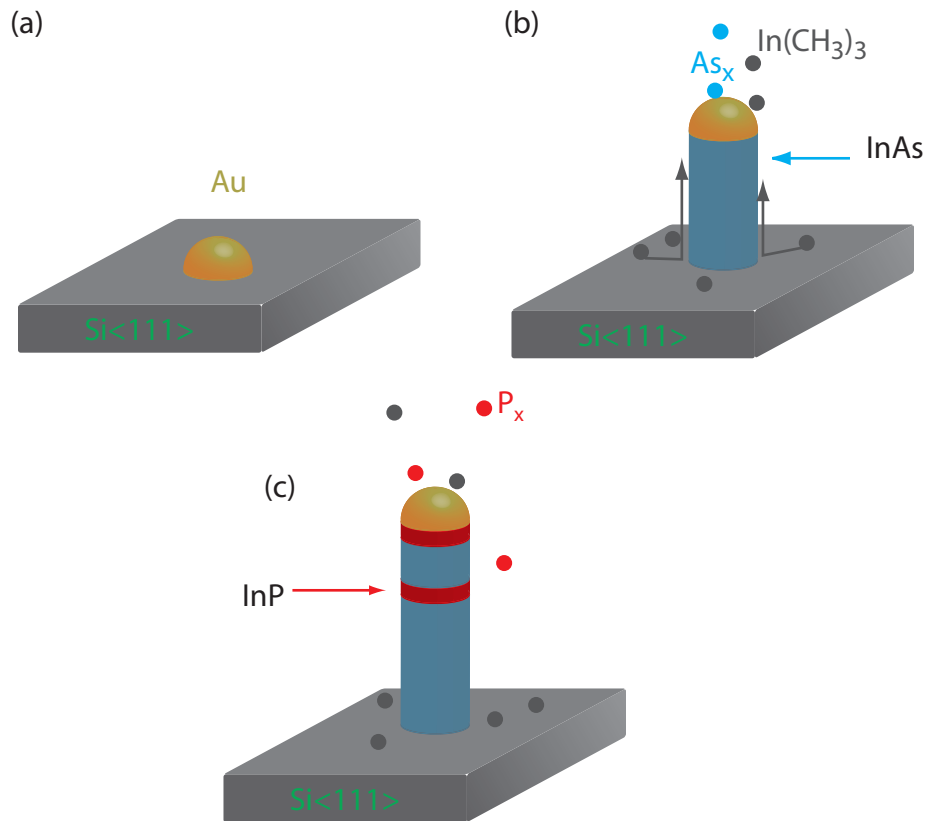
Figure 3.1. (a) Au seed particles are deposited onto a Si<111> substrate. (b) The growth species are introduced into the chamber. (c) The heterostructure nanowire is achieved by alternating the growth species from As to P during the growth process. Figure based on Figs. 2.1 and 2.5 in Ref. [34].

Quantum Dot Circuitry

After InAs/InP nanowires are made, the next step is to make metal contacts to the wire for electrical measurements. Figure 3.2 is a schematic of the resulting device. The procedure for contacting the nanowires is as follows [37, 39]. First the nanowires are deposited onto a conducting n-doped silicon wafer. This portion of wafer serves as a global back-gate. This wafer is capped with a 100 nm layers of SiO_x to insulate

the nanowires from the back-gate. Then Ni and Au are evaporated through a shadow mask to make bond pads for wire bonding.
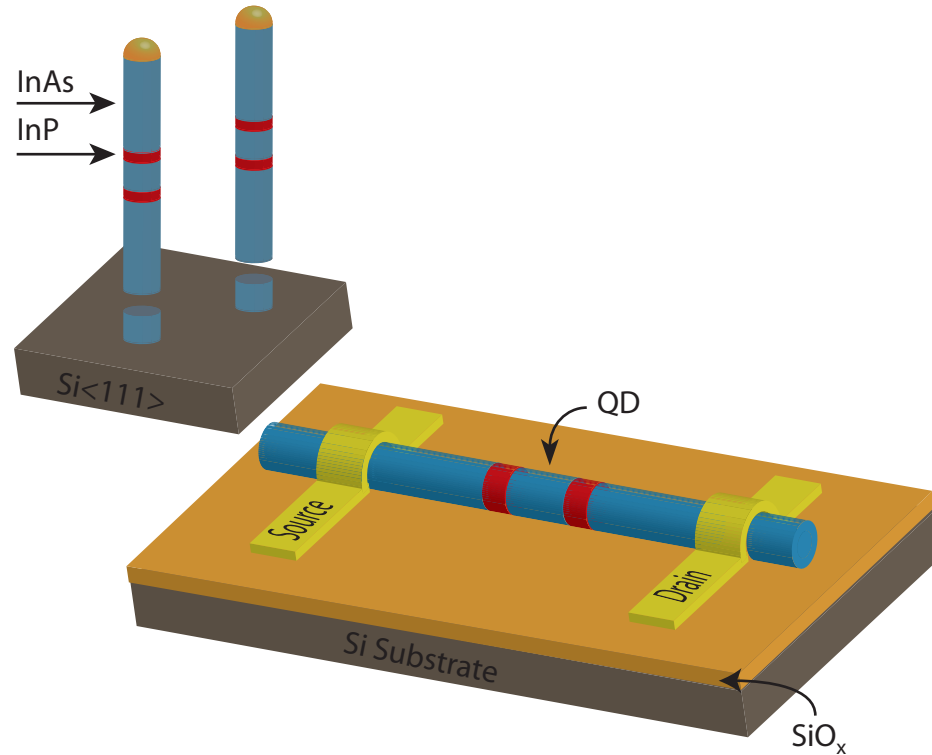
Figure 3.2. The nanowires on the growth substrate are transferred to the growth substrate consisting of an insulating SiO_x layer on top of a conductive n-doped Si layer, which serves as a global back-gate. Au/Ni metallic leads are defined using EBL and subsequent metallization to create Ohmic contacts to the nanowires. The wires are made from InAs (blue) and the barriers are from InP (red). The quantum dot (QD) is then defined by the double barriers.

Once these large bond pads are ready, the InAs/InP nanowires are removed from their growth substrate by gently sweeping with a clean room tissue and then transferred to the measurement wafer. This wire deposition is random. But the nanowires can be located using an optical microscope. Next PMMA resist is spin coated to cover the entire substrate. At this point, the ohmic contacts for each wire

are designed manually. These small-scale contacts (100s of nm) are defined using electron beam lithography (EBL). After EBL exposure, the sample is developed in MIBK/IPA solutions. An ozone etch is performed to remove residual resist and other organic contamination. Because the nanowire surfaces oxidize when exposed to atmosphere, prior to metallization, the wires are passivated in NH_4S_x to remove the native oxide. Then 25 nm of nickel and 90 nm of gold are subsequently evaporated followed by a lift off in heated acetone to remove the remaining PMMA and metals. The resulting device is shown schematically in Fig. 3.2.

<u>Experimental Setup</u>

Basic Characterization

After the wire is connected with the metal contacts, basic device characterizations such as IV measurements can be performed. By definition, the differential conductance, G, is the change in current, dI, in response to an infinitesimal change in voltage, dV, this is $G = dI/dV$. In the experiments, G is measured by applying a finite but small voltage, δV, usually smaller than thermal energy kT, and then measuring the change in the current , δI. The measurement is best done using a lock-in technique and an ac bias voltage. This lock-in technique improves the signal-to-noise ratio because noise at frequencies other than that of the applied ac voltage will be attenuated.

The most complete differential conductance measurement is the so-called Coulomb-blockade spectroscopy measurement, which maps out the differential conductance as

a function of gate and dc bias voltage. Experimentally, the ac and dc biases are applied simultaneously using a mixing circuit (see Fig. 3.3).

The ratio V_{out}/V_{in} can be approximated by $R_G/(R_G + R_{in})$ for $R_G \ll R_{NW}$ where R_G, R_{in} and R_{NW} are the resistance to ground, the input resistance and the nanowire resistance, respectively. The ac and dc inputs are supplied by the lock-in amplifier, Stanford Research System (SRS) model 830, and a power supply Yokogawa 7651, respectively. The gate voltage connecting to the back of the Si substrate is generated by a separate power supply (Yokogawa model 7651). The preamplifier (SRS570) is connected to the drain side of the nanowire and produces a voltage proportional to the input current (see Fig. 3.4). This preamplifier also provides the electrical ground for the entire setup. The output ac and dc voltages from the preamplifier are then feed into the lock-in amplifier (SRS 830) and into a digital multimeter to measure the ac and dc components, respectively.

Heat Source

In order to perform a thermoelectric experiment, there must be a heat source to establish a temperature gradient across the device. In order to achieve this goal, the source and drain contacts are designed in a 'T'-shape, see Fig. 3.5(a). The top bar of the 'T' provides the path for heating current. It is made thin at the middle portion to increase the resistance, hence raising the electron temperature. The heating circuit has independent inputs for heating and biasing voltage. It splits the input ac heating voltage into two voltages, $v_{\pm}$, which have equal magnitudes and opposite signs. The
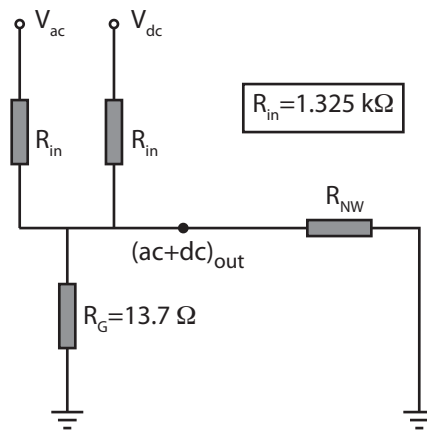
Figure 3.3. A mixing circuit combines ac and dc voltages together. R_G is the resistance to ground, R_{in} is the input resistance, and R_{NW} is the nanowire resistance. $R_G/(R_G + R_{in})$ is 0.01 for both ac and dc components.
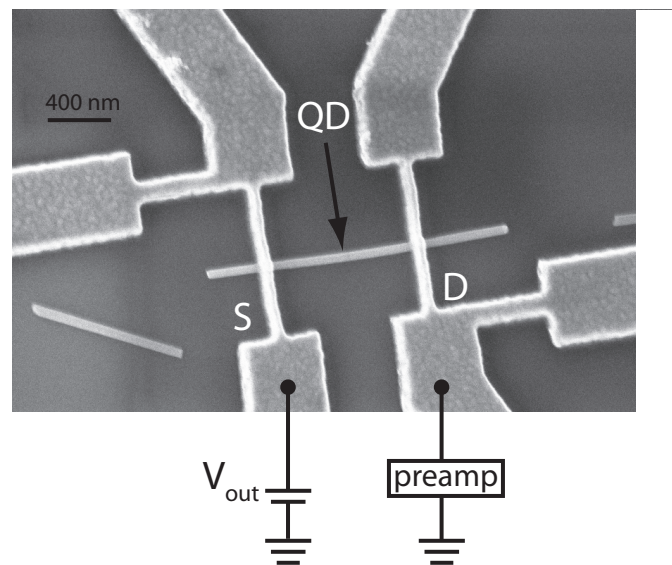
Figure 3.4. A scanning electron microscope image of a nanowire device contacted at both ends. The quantum dot (QD) is not seen at this magnification. S and D indicate the source and drain contacts. The 'T' shape contacts are for heating (see text). The bias voltage, V_{out}, is supplied by a mixer circuit (see Fig. 3.3). The current preamplifier, which provides the path to ground, creates a voltage proportional to the input current. This voltage then feeds into the lock-in amplifier (ac) and digital multimeter (dc).

third leg (p) provides the electrical balance (probe). A trimming circuit provides the ability to tune $v_\pm$ such that at the nanowire the two voltages cancel, $v_+ + v_- = 0$ (see Fig. 3.5(b)). As a result, the current created by $v_\pm$ heats the electrons in the source contact without electrically biasing the quantum dot.
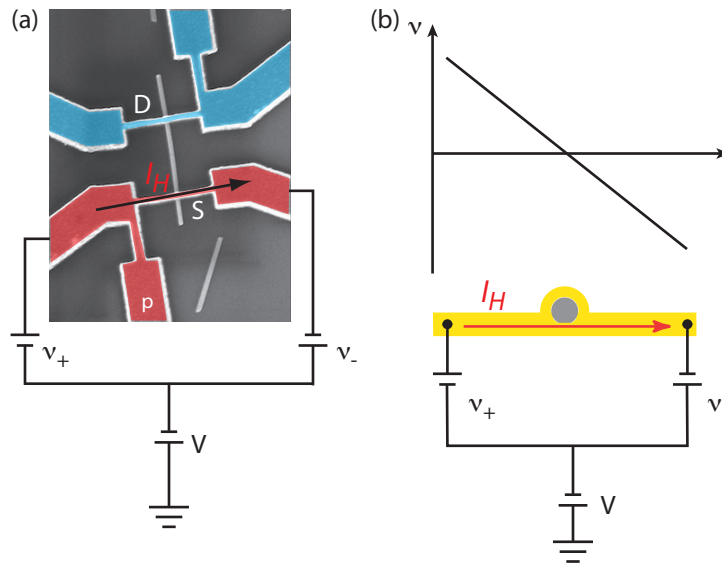
Figure 3.5. (a) An SEM image of a nanowire with 'T'-shape source and drain contacts. The heating current, I_H, flows through the source contact without biasing the nanowire. This is achieved by using two op-amps to generate v_+ and ν_-. (b) A side-view of the heating channel. A voltage probe (p) provides fine tuning to ensure that the two signals cancel each other at the nanowire.

All thermoelectric experiments are performed using a low-frequency ac heating current (17 Hz). Apart from increasing the signal-to-noise ratio as mentioned previously, the benefit of using an ac heating current and lock-in techniques is that the resulting ac thermal gradient is frequency doubled. This means that measurements are performed at a separate frequency from the applied heating current. This separation helps isolate measurements from any noise created by the heating current. To see why

this is true, consider the temperature difference, ΔT, created by the heating current, $I_H = cos(wt)$,

$$\Delta T \propto P_{Joule} = I_H^2 R \propto \cos^2(\omega t) \propto \cos(2\omega t) \tag{III.1}$$

Hence electron transport induced by ΔT will appear at the second harmonic, 2ω (34 Hz in our case).

Thermoelectric Property Measurements

Thermocurrent

The thermocurrent, I_{th}, is the electrical current that flows in response to the temperature difference, ΔT. The thermocurrent is given by $I_{th} = G_{th}\Delta T$, where G_{th} is the thermoelectric coefficient indicating how much current can flow as a result of the temperature difference. In order to measure I_{th}, the heating current is applied at the source contact and, using a lock-in technique, the frequency-doubled current is measured via the preamplifier. The net current flow through the dot is

$$I(t) = GV + Gv\cos(\omega t) + G_{th}\Delta T(t), \tag{III.2}$$

where V is bias voltage and $v\cos(\omega t)$ accounts for any voltage noise at frequency w. Because thermal effects are expected at the second harmonic (2ω), thermocurrent can be written as $I_{th} = I_0\cos(2\omega t)$, where I_0 is the amplitude of the ac thermocurrent. Thus the net current becomes

$$I(t) = GV + Gv\cos(\omega t) + I_0\cos(2\omega t). \tag{III.3}$$

The internal circuitry of the lock-in amplifier extracts I_0 from the total current $I(t)$ by integration. The orthogonal property of the cosine function causes other terms except $\cos(2\omega t)$ to vanish. The lock-in performs the following calculation

$$
\begin{aligned}
\frac{\omega}{\pi} \int_0^\tau I(t) \cos(2\omega t) dt &= \frac{\omega}{\pi} \int_0^\tau [GV + Gv \cos(\omega t) + I_0 \cos(2\omega t)] \cos(2\omega t) dt \\
&= \frac{\omega}{\pi} I_0 \int_0^\tau \cos^2(2\omega t) dt \\
&= I_0.
\end{aligned}
$$

To measure I_0, the lock-in amplifier generates the signal with 2ω frequency and averages the signal over a period. The orthogonal property of the cosine function ensures that the first two terms of the integration are zero. Thus the measurement is insensitive to $v \cos(\omega t)$. Further details of the thermocurrent experiment can be found in Ref. [40].

Thermovoltage, V_{th}

Ideally, to measure thermovoltage, the input impedance of the measurement instrument should be infinitely large. In our lab, the low-noise voltage preamplifier (Femto DLVPA-100-F-D series) with FET input stage has an input impedance of 1 TΩ.

In a current measurement, the drain contact is connected to the ground (via the current preamplifier) while the source contact is attached to the output voltage of the mixer circuit, V_{out}. A change in gate voltage has insignificant influence on the voltage of the source and drain since both ends of the wire are pinned to fixed voltages. However, in the true open circuit measurement, the drain contact is disconnected. As

a result V_D is floating and may be affected by the gate voltage. The source side is pinned by the bias while the drain voltage V_D changes as gate voltage changes. As a result, V_D biases the wire and a current will flow as the system tries to reach the equilibrium. In essence, the gate voltage obscures the true open circuit voltage by creating an additional voltage.

This problem can be lessened by attaching a load resistance between the drain contact and ground. This reduces the gate-induced voltage by providing a path to ground. This gate-induced voltage is measured under isothermal conditions then subtracted from the thermovoltage measurements. Now what is being measured is not thermovoltage but the voltage across the load resistor (see Fig. 3.6). The true thermovoltage is

$$V_{th} = I(R_L + R) = V_L \left(1 + \frac{R}{R_L}\right), \tag{III.4}$$

where $R = 1/G$ is the resistance of the dot. This becomes complicated because this resistance is also a function of gate voltage. However, when $R_L \gg R$, the thermovoltage can be approximated by V_L. More details on the thermovoltage measurements can be found in Ref. [40].
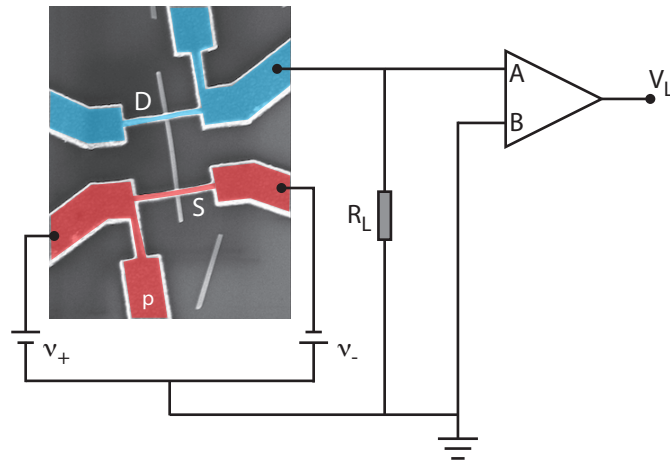
Figure 3.6. A schematic of the setup used for thermovoltage measurements. V_L is measured which can be made close to thermovoltage if $R_L \gg R$, see Eq. III.4.

CHAPTER IV

MEASURING A TEMPERATURE DIFFERENCE ACROSS A QUANTUM DOT

In order to measure the thermoelectric properties of a quantum dot, not only the absolute ambient temperature is required, but also the electron temperature difference across the dot. In this chapter, a method to measure a temperature difference across a quantum dot is presented. The measurements reported in this chapter were done by Eric A. Hoffmann. The author has contributed to the modeling and the derivation in the narrow width regime, $\Gamma \ll kT$ (see text).

Introduction

In thermoelectric experiments, one needs to establish and measure a temperature difference across the device. One way to achieve this is to heat a heating module consisting of a resistor. The same resistor can then be used to measure the temperature of the lattice [41]. But at low temperature, the lattice temperature can be quite different from the electron temperature. Another method includes employing a quantum point contact to measure voltage across a heating channel defined in a two-dimensional electron gas using a known Seebeck coefficient [42].

A new method for measuring a temperature gradient was developed during this thesis and uses a quantum dot as a thermometer [43–46]. The quantum dot with

its unique energy-dependent transmission function can be used as a tool to sense the Fermi-Dirac distribution of the electron gas where temperature strongly affects the profile of the distribution. However, the transmission is not known a priori. By measuring the thermocurrent I_{th} and the differential conductance G, the temperatures can be extracted by comparing the two measurements (one with heating and one without). This technique requires that the energy spacing in the dot is greater than the thermal energy, $\Delta E \gg kT$. This can be achieved easily in a nanowire-based double-barrier quantum dot working in the Coulomb blockade regime where $E_C \gg kT$.

Once a heating current is applied to the source contact, the temperature profile along the wire looks like the one shown in Fig. 4.1. The ambient temperature, T_0, is the temperature of the cryostat and $\Delta T_{H,C}$ are the temperature rises on the hot and cold sides of the dot, respectively. This thermometry method can be used to measure $\Delta T_{H,C}$ separately by applying appropriate bias and gate voltages so that only one of the electrochemical potentials is near the dot resonant level (see Fig. 4.2).

<p style="text-align:center">Theoretical Consideration</p>

The thermocurrent is the net current flow as a result of a temperature gradient across the dot. Starting from the two-terminal Landauer equation for current [27],

$$I = -\frac{2e}{h} \int [f_H(E) - f_C(E)] \tau(E) dE, \qquad \text{(IV.1)}$$
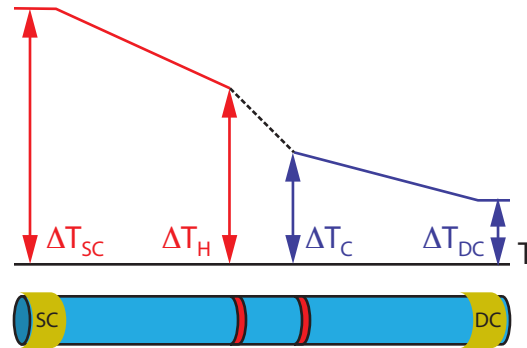
Figure 4.1. The temperature profile along a nanowire heated at one end, at low temperatures. T is the ambient temperature. When the heating current is applied at the source contact (SC) the electron temperature rises above T by an amount of ΔT_{SC}. The associated temperature rise at the drain contact is ΔT_{DC}. At the barriers, the rises in electron temperatures are denoted ΔT_H and ΔT_C .
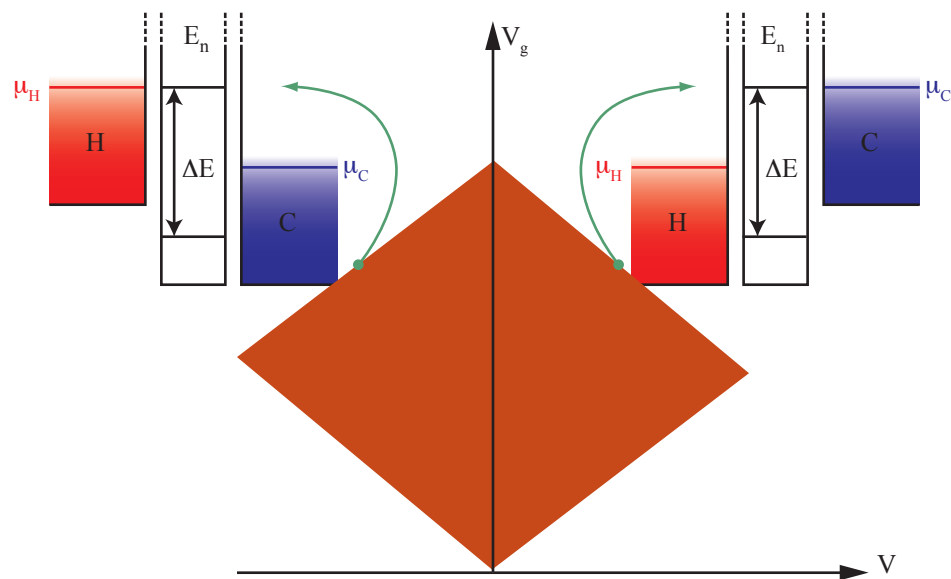
Figure 4.2. The energy diagram shows the bias and gate voltages which set $\mu_{H,C}$ closer to the resonance while the other electrochemical potential is many kT away. This requires the energy spacing to be larger than the thermal energy, $\Delta E \gg kT$

the thermocurrent can be written as

$$I_{th} = \Delta T \frac{\partial I}{\partial T} = -\Delta T \frac{2e}{h} \int \frac{\partial (f_H - f_C)}{\partial T} \tau(E) dE. \tag{IV.2}$$

When only one of the electrochemical potentials is near the resonance (see Fig. 4.2), this current can be written as

$$I_{th}|_{H,C} = \mp \Delta T_{H,C} \frac{2e}{h} \int \frac{\partial f_{H,C}}{\partial T_{H,C}} \tau(E) dE$$

$$= \Delta T_{H,C} \frac{2e}{h} \int F_{H,C}(E) \tau(E) dE, \tag{IV.3}$$

where

$$F_{H,C}(E) = \mp \frac{\partial f_{H,C}}{\partial \xi_{H,C}} \frac{\partial \xi_{H,C}}{\partial T_{H,C}} = \pm \frac{\partial f_{H,C}}{\partial \xi_{H,C}} \frac{\xi_{H,C}}{T_{H,C}}. \tag{IV.4}$$

Even though the thermocurrent (Eq. IV.3) provides information about the temperature of incoming electrons, this is not enough to determine $\Delta T_{H,C}$ because the Fermi-Dirac function is convoluted with the transmission function. However, in combination with the second differential conductance, $\Delta T_{H,C}$ can be measured.

Consider the second differential conductance, denoted by $G_2 = d^2 I/dV^2$, at the same bias and gate voltages configuration,

$$G_2 = \frac{\partial^2 I}{\partial V^2} = \mp \frac{2e}{h} \int \frac{\partial^2 f_{H,C}}{\partial V^2} \tau(E) dE. \tag{IV.5}$$

The first and second derivatives of $f_{H,C}$ with respect to V can be written as [40],

$$\frac{\partial f_{H,C}}{\partial V} = \frac{\partial f_{H,C}}{\partial \xi_{H,C}} \frac{\partial \xi_{H,C}}{\partial V}$$

$$= \left(\frac{\pm e}{2kT_{H,C}}\right) \frac{\partial f_{H,C}}{\partial \xi_{H,C}}$$

$$\frac{\partial^2 f_{H,C}}{\partial V^2} = \left(\frac{\pm e}{2kT_{H,C}}\right) \frac{\partial^2 f_{H,C}}{\partial \xi_{H,C}^2} \frac{\partial \xi_{H,C}}{\partial V}$$

$$= \left(\frac{\pm e}{2kT_{H,C}}\right)^2 \frac{\partial^2 f_{H,C}}{\partial \xi_{H,C}^2}.$$

And the first and second derivatives of $f_{H,C}$ with respect to $\xi_{H,C}$ are given by,

$$\frac{\partial f_{H,C}}{\partial \xi_{H,C}} = -f_{H,C}^2 \exp(\xi_{H,C})$$

$$\frac{\partial^2 f_{H,C}}{\partial \xi_{H,C}^2} = -2f_{H,C} \frac{\partial f_{H,C}}{\partial \xi_{H,C}} \exp(\xi_{H,C}) - f_{H,C}^2 \exp(\xi_{H,C})$$

$$= \frac{\partial f_{H,C}}{\partial \xi_{H,C}} (1 - 2f_{H,C} \exp(\xi_{H,C}))$$

$$= \frac{\partial f_{H,C}}{\partial \xi_{H,C}} \left(1 - \frac{2\exp(\xi_{H,C})}{1 + \exp(\xi_{H,C})}\right)$$

$$= \frac{\partial f_{H,C}}{\partial \xi_{H,C}} \left(\frac{1 - \exp(\xi_{H,C})}{1 + \exp(\xi_{H,C})}\right)$$

$$= \frac{\partial f_{H,C}}{\partial \xi_{H,C}} (2f_{H,C} - 1).$$

Inserting this into Eq. IV.5 gives

$$\frac{\partial G}{\partial V} = -\frac{2e}{h} \left(\frac{e^2}{4k^2 T_{H,C}}\right) \int M_{H,C}(E)\tau(E)dE, \qquad (IV.6)$$

where

$$M_{H,C}(E) = \pm \frac{\partial f_{H,C}}{\partial \xi_{H,C}} \left(\frac{2f_{H,C} - 1}{T_{H,C}}\right) \qquad (IV.7)$$

The integrand of thermocurrent and second differential conductance bear some similarity. This can be seen in the plot of those two equations (for example see figure

4.3). This is the reason why the second differential conductance is used instead of the conventional differential conductance. Using these two quantities, it is possible to extract temperature at the source(drain) side of the quantum dot from the ratio, defined as

$$R_{H,C} \equiv \left(\frac{I_{th}}{G_2}\right)\Big|_{H,C},\qquad(IV.8)$$

when only the electrochemical potential of the source (drain) side alone is near the resonant level of the dot.
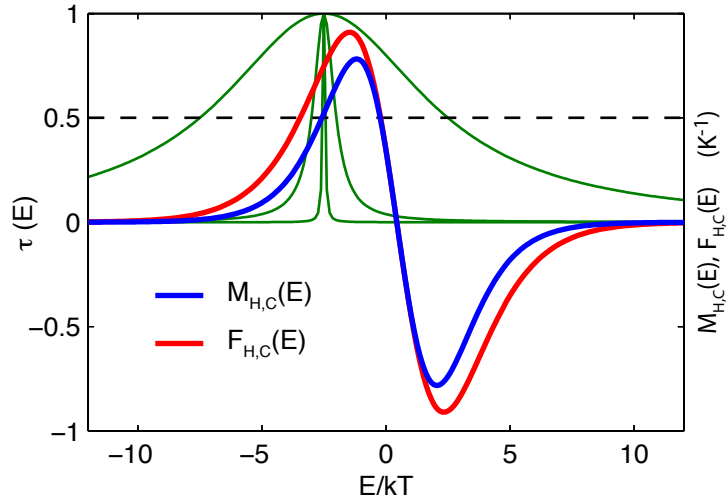
Figure 4.3. Plot of functions $F_{H,C}(E)$, $M_{H,C}(E)$, for fixed μ and V, as a function of E/kT. The transmission function $\tau(E/kT)$ (green color) with $\Gamma = 10kT, kT$, and $0.1kT$ is also plotted. The width of the transmission function determines which range of $F_{H,C}, M_{H,C}$ will contribute to the ratio $R_{H,C}$.

The transmission function plays an importance role in thermometry of a quantum dot, because it controls which electrons can tunnel through the dot. In the Lorentzian approximation, it can be characterized by the full width at half maximum, denoted by Γ. However, the finite width can be considered narrow or broad only relative to

the thermal energy, kT. In the following subsections, the thermometry in the limit of narrow and broad transmission width will be discussed.

Measurements of I_{th} and G_2 reflect the convolution of $F_{H,C}$ and $M_{H,C}$ with $\tau(E)$. As shown in Fig. 4.3, this convolution means that the transmission width influences how the two functions $F_{H,C}$ and $M_{H,C}$ will contribute to the ratio $R_{H,C}$. In the case of narrow width, only a small region near the peak resonance (at $E = E_0$) can contribute significantly. In the limit of a delta function, the values of these two functions at $E = E_0$ determine the ratio and lead to the analytical limit of $R_{H,C}$. For the broad-width regime, $\Gamma \gg kT$, a larger range contributes nearly equally to the ratio. After the contribution has been numerically calibrated, $\Delta T_{H,C}$ can be determined directly from the ratio $R_{H,C}$.

$$\text{Narrow Transmission Width Regime, } \Gamma \ll kT$$

For the narrow-width limit, the transmission function can be approximated as a Dirac delta function with an unknown amplitude, $\tau(E) = A\delta(E - E_0)$, where E_0 is the resonant level of the dot and A is the unknown amplitude of the transmission function. Equations IV.3 and IV.5 can now be written as

$$I_{th}\Big|_{H,C} = A\Delta T_{H,C} \frac{2e}{h} \frac{\partial f_{H,C}}{\partial \xi_{H,C}} \frac{\xi_{H,C}}{T_{H,C}}\Big|_{E=E_0} \tag{IV.9}$$

$$G_2 = A\frac{2e}{h}\left(\frac{e^2}{4k^2 T_{H,C}}\right)\frac{\partial f_{H,C}}{\partial \xi_{H,C}}\left(\frac{2f_{H,C} - 1}{T_{H,C}}\right)\Big|_{E=E_0} \tag{IV.10}$$

Using Eq. IV.9, the ratio is approximated as

$$
\begin{aligned}
R_{H,C}^{<} &= \left. \frac{\Delta T_{H,C} \frac{\xi_{H,C}}{T_{H,C}}}{\frac{e^2}{4k^2 T_{H,C}^2}(2f_{H,C}-1)} \right|_{E=E_0} \\
&= \left. \Delta T_{H,C} \frac{4k^2}{e^2} T_{H,C} \frac{\xi_{H,C}}{2f_{H,C}-1} \right|_{E=E_0} \\
&= \left. \Delta T_{H,C} \left(\frac{4k^2}{e^2} \right) T_{H,C} \left(\frac{\xi_{H,C})}{\frac{2}{1+\exp(\xi_{H,C})} - \frac{1+\exp(\xi_{H,C})}{1+\exp(\xi_{H,C})}} \right) \right|_{E=E_0} \\
&= \left. \Delta T_{H,C} \left(\frac{4k^2}{e^2} \right) T_{H,C} \left(\xi_{H,C} \frac{1+\exp(\xi_{H,C})}{1-\exp(\xi_{H,C})} \right) \right|_{E=E_0} \\
&= \left. \Delta T_{H,C} \left(\frac{4k^2}{e^2} \right) T_{H,C} \left(\xi_{H,C} \coth \left(\frac{\xi_{H,C}}{2} \right) \right) \right|_{E=E_0} \quad \text{(IV.11)}
\end{aligned}
$$

The electrochemical potentials can be expressed in voltage as $V_{H,C}^0 = \mp 2(E_0 - \mu)/e$.

Then $\xi_{H,C}$ becomes

$$
\xi_{H,C}\big|_{E=E_0} = \frac{e}{2} \left(\pm \frac{V - V_{H,C}^0}{k T_{H,C}} \right)
$$

The ratio can be written as,

$$
R_{H,C}^{<} = \Delta T_{H,C} \left(\frac{2k}{e} \right) (V - V_{H,C}^0) \coth \left(\frac{e}{4k} \frac{V - V_{H,C}^0}{T + \Delta T_{H,C}} \right) \quad \text{(IV.12)}
$$

where $V_{H,C}^0$ are measured experimentally by locating the bias of the zero-point crossings.

With this equation, $R_{H,C}^{<}$ can be used to fit the ratio, R, of measured thermocurrent

and second conductance with the temperature rise, $\Delta T_{H,C}$, used as fitting parameters

[40, 45, 46].

Broad Transmission Width Regime, $\Gamma \gg kT$

In this regime, the key for extracting temperature rise is that there is the similarity

between $F_{H,C}$ and $M_{H,C}$ [40, 43, 44]. To illustrate the point, consider $M_{H,C}(E)$ at the
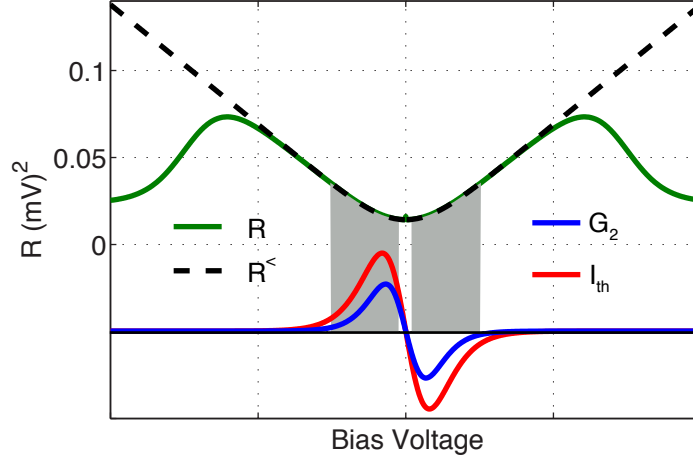
Figure 4.4. Simulated thermocurrent (red) and the second differential conductance (blue) with $\Gamma \ll kT$. The ratio, R, (green, Eq. IV.8) of the two and $R^<_{H,C}$ (dashed line, Eq. IV.12) are shown at the top. Note the range of bias voltage where $R^<_{H,C}$ overlaps with R and coincides with the range where I_{th} and G_2 have peak signals (grey area). This is where the data will be collected. In the measurements, this range provides a good signal-to-noise ratio.

limit of $\xi_{H,C} \to 0$,

$$M_{H,C} = \pm \frac{\partial f_{H,C}}{\partial \xi_{H,C}} \frac{2f_{H,C}-1}{T_{H,C}} \approx -\frac{\partial f_{H,C}}{\partial \xi_{H,C}} \frac{\xi_{H,C}}{2T_{H,C}} = F_{H,C}/2.$$

This is also true at other values of $\xi_{H,C}$ as $\dfrac{\partial f_{H,C}}{\partial \xi_{H,C}}$ becomes vanishingly small. So when

$\xi_{H,C}$ is small, I_{th} is proportional to G_2. Hence, the thermocurrent can now be written

as,

$$I_{th}\big|_{H,C} = \Delta T_{H,C} \left(\frac{2e}{h}\right) \int F_{H,C}(E)\tau(E)dE$$

$$\approx -\Delta T_{H,C} \left(\frac{2e}{h}\right) \int 2M_{H,C}(E)\tau(E)dE. \tag{IV.13}$$

Using Eq. IV.13 for I_{th} and Eq. IV.6 for G_2, then the ratio becomes

$$R \approx T_{H,C} \frac{\Delta T_{H,C}}{\Lambda_{H,C}} \left(\frac{4k^2}{e^2}\right) \tag{IV.14}$$

where $\Lambda_{H,C}$ is a unitless parameter introduced to correct an error associated with the approximating of $F_{H,C}$ as $M_{H,C}$, and it also absorbs a factor of 2 in the integrand of Eq. IV.13. Solving this equation for $\Delta T_{H,C}$ gives

$$\Delta T_{H,C} = \pm \frac{1}{2} \sqrt{T^2 + \Lambda_{H,C} \frac{e^2}{2k^2} R} - \frac{T}{2}. \qquad (IV.15)$$

In the broad width regime, the ratio R, usually forms a plateau around $V_{H,C}^0$ (see Fig. 4.5). This plateau is suitable to determine $\Delta T_{H,C}$. To determine the temperature rise, data points in this range are fed into Eq. IV.15 along with $\Lambda_{H,C}$, which is calculated separately, and the ambient temperature and then averaging over the data set to obtain the temperature rise.
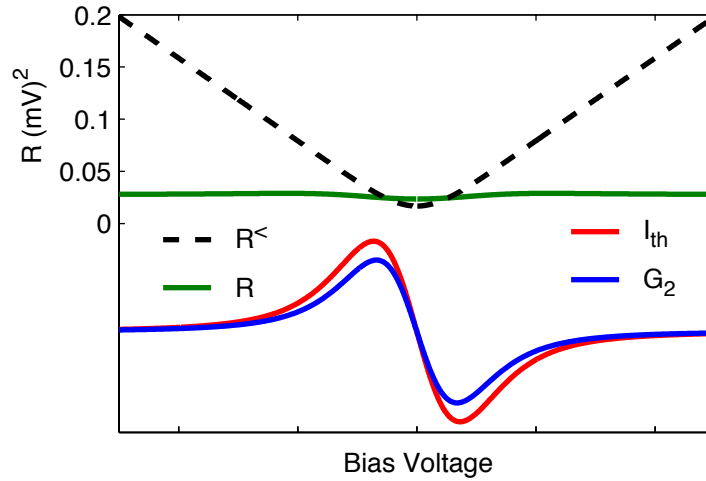
Figure 4.5. A plot of a numerical calculation of the ratio R (green, Eq. IV.8) for $\Gamma = 10kT$. The blue and red lines are numerical calculations of I_{th} and G_2 with arbitrary units, respectively. The dashed line is $R_<$ for $\Gamma \ll kT$ (Eq. IV.12). For $\Gamma \gg kT$, the ratio forms a plateau and Eq. IV.12 can not be used to predict ΔT.

Figure 4.6 displays the simulated data of $\Delta T_{H,C}$ as a function of ΔT_{SC}. This figure shows that results obtained from Eq. IV.15 for the broad-width regime agree

with true values (solid line) up to $\Delta T_H / T = 10$. This is beyond the intended limit as most experiments are below $\Delta T_H / T = 2$ limit. In this figure, it is clear that Λ is quite insensitive to the exact value of Γ.
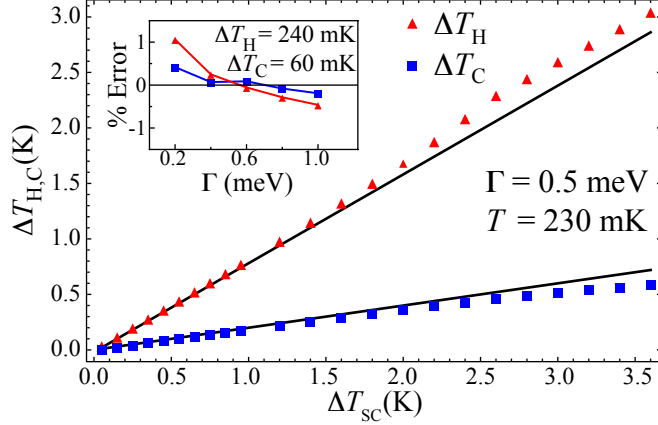
Figure 4.6. A plot of simulated data of $\Delta T_{H,C}$ as a function of ΔT_{SC} at $T = 230$ mK and $\Lambda = \Lambda_{H,C}$. Simulated data agree with the true value (solid line) up to $\Delta T_H / T = 10$. Inset: The percent error as a function of Γ as a particular temperature rises. The error is within 1 % over an order of magnitude in Γ.

Measurements and Results

This data is then used for comparison with the numerical simulation (done by the author as part of this dissertation). The first step in the experiment is to find a suitable gate voltage where a quantum dot is not influenced by the excited states or other second-order effects. This is accomplished by using Coulomb blockade (CB) measurement, (for example see Fig. 2.3). The CB diamond provides information about which diamond (resonant level) is a good candidate for a well-separated resonance energy. Then high-resolution bias voltage sweeps of thermocurrent and differential

conductance locate gate voltages. Fig. 4.7(a) illustrates numerically the ideal behaviors as a function of bias voltage where both signals have similar curves and the ratio R forms a trough. Once this gate voltage has been found, the measurement of thermocurrent and differential conductance can proceed [40].

The thermocurrent and differential conductance are measured simultaneously. This means that the inputs for both measurements must be combined. The ac + dc biases are joined together using the voltage adder (see Sec. 3.2). This input is then added to the ac heating voltage from the heating box. The ac bias and ac heating frequencies are set at 42 Hz and 17 Hz, respectively. These frequencies were chosen to avoid the slow time constant due to the high impedance of the device. These frequencies are fast enough to take the advantage of the lock-in amplifier and are kept away from multiples of 60 Hz (power line frequency). The conductance and thermocurrent are measured at the 42 Hz and 34 Hz (the second harmonic of the heating current as discussed in chapter II) using separate lock-in amplifiers. The second differential conductance is obtained from the numerical derivative of the measured conductance, dG/dV.

After the data has been collected, the analysis starts by determining which regime Γ is in. The devices used in the lab have relatively thick barriers which makes Γ narrow. This makes them fall into the narrow-width regime. This is confirmed by fitting the measure differential conductance peak. Another indication is that the ratio R (Eq. IV.8) forms a trough where signals locate, as expected from Fig. 4.4 (see

Fig. 4.7(a) for data). Hence the data is analyzed using Eq. IV.12. Around the voltage where I_{th} and G_2 cross through the zero, the ratio of I_{th} and G_2 becomes unreliable as a result of a numerical division-by-zero error as shown in Fig. 4.7(b). Instead of excluding these data points, a histogram of resulting $\Delta T_{H,C}$ is employed to determine the mean value of $\Delta T_{H,C}$ (see Fig. 4.8(b)). In this way, the anomaly becomes outlier points and has insignificant influence on the mean value.

To get the resulting $\Delta T_{H,C}$, R data points are fed into Eq. IV.12, and then the transcendental function is solved numerically. Each data point gives one value of corresponding $\Delta T_{H,C}$ and these are then binned to form a histogram. The mean value is determined statistically from the histogram, and an error bar is determined by finding the range of $\Delta T_{H,C}$ which covers 67% of all the data points. Normally the error bars are asymmetric about the mean. To verify that the obtained mean value is reasonable, $R_{H,C}^{<}$ is plotted using the mean value over the measured value as shown in Fig. 4.8. After the data sets for various heating currents have been collected and analyzed, the temperature rises on hot and cold sides as well as the temperature difference can be plotted as a function of heating current as shown in Fig. 4.9

This method of measuring temperature rises on both hot and cold sides of a quantum dot provides an essential tool for the thermoelectric study of quantum dots. It could be used in thermal transport of quantum dots as well. It has been used in our lab for other experiments such as measuring nonlinear thermoelectric effects.
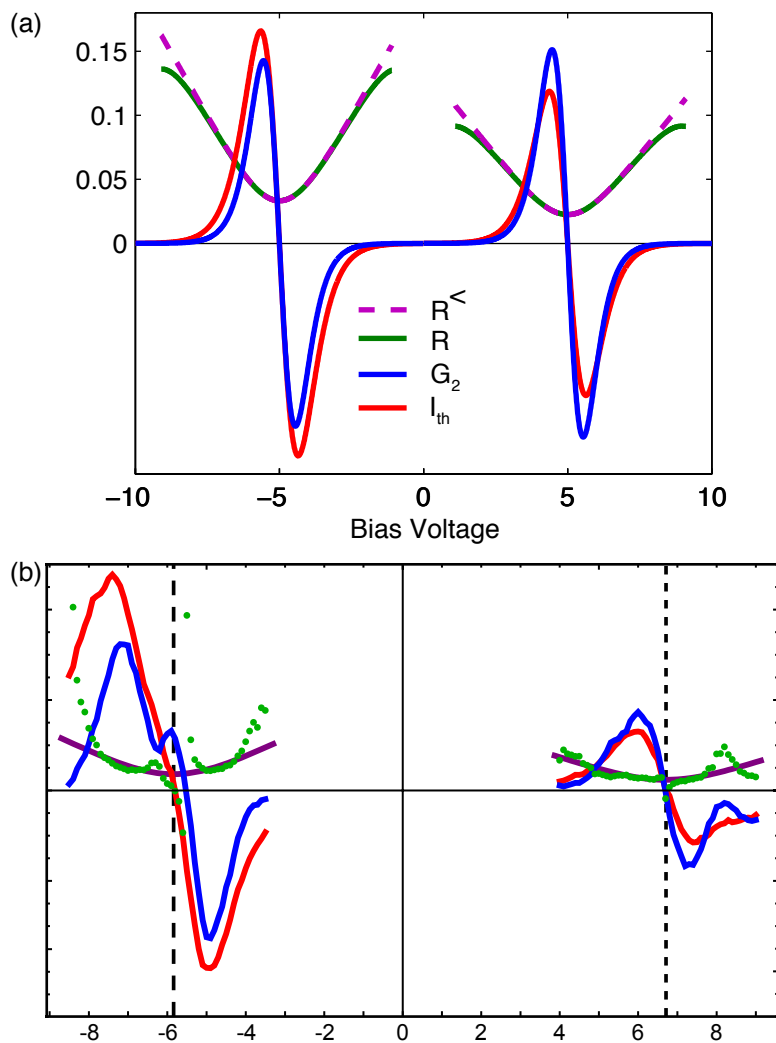
Figure 4.7. (a) A numerical simulation of I_{th} and G_2 and its ratio as a function of bias voltage for $\Gamma = 10$ μeV and $T = 2.2$ K ($kT = 190$ μeV). R (green) is the ratio and $R_<$ is the result from Eq. IV.12. (b) Example of experimental data of I_{th} (red) and G_2 (blue) and their ratio R (green). The experiment was done at $T = 2.2$ K and $I_H = 150$ μA. The fitting function, $R^<_{H,C}$ (Eq. IV.12), gives $\Delta T_H = 230$ mK and $\Delta T_C = 160$ mK.
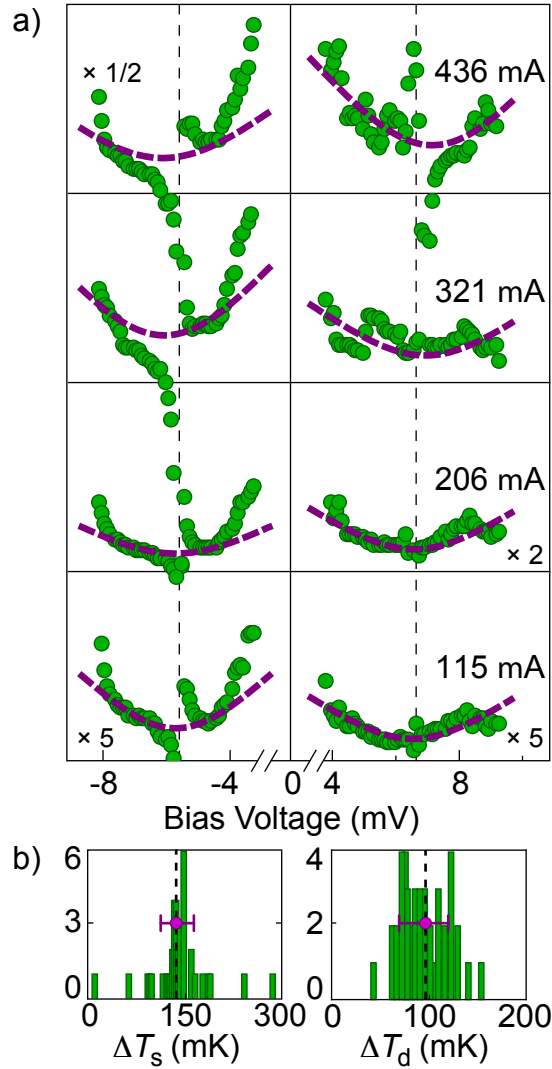
Figure 4.8. (a) The data point for R (green dots) measured at four different heating current, I_H and at $T = 2.94$ K. The left column determines ΔT_H and the right column determines ΔT_C. The dashed lines are calculated from Eq. IV.12. (b) Histograms of data from $I_H = 115~\mu$A. The dots mark the mean value of $\Delta T_{H,C}$ and the error bars encompass 67% of the entire data points.
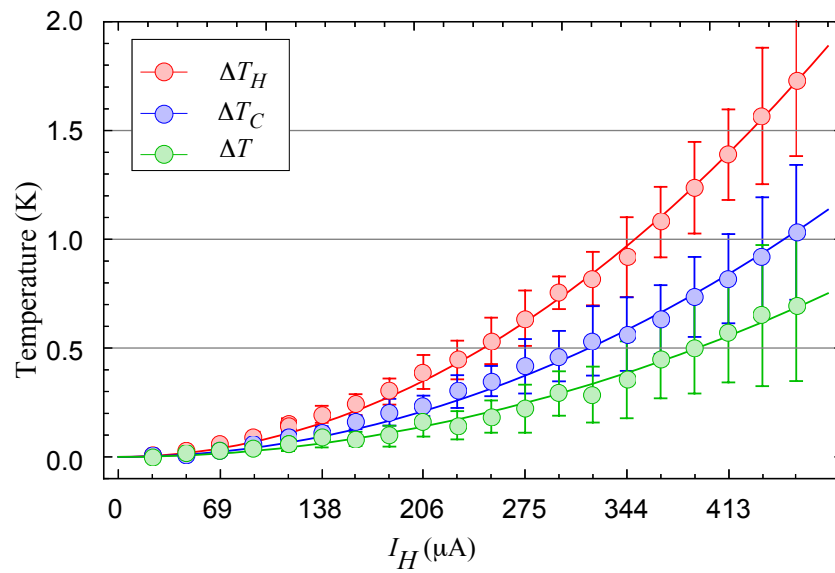
Figure 4.9. A plot of temperature rises and temperature difference as a function of heating current from experimental data (circles). The solid lines are second-order fits of the data. The measurement was done at $T = 2.94$ K.

CHAPTER V

NONLINEAR THERMOELECTRICS

Introduction

The experimental data used in Fig. 5.1 was measured by the author while data used in Figs. 5.2 and 5.4 was measured by Eric Hoffmann. The numerical and theoretical analysis was done by the author.

Low-dimensional devices such as quantum dots have been proposed for thermoelectric power generators and refrigerators [15, 47–49]. Nonlinear effects could affect the performance of these devices. Thus a better understanding of these effects would be helpful in order to achieve the highest performance. It is the goal of this chapter to observe and understand strong nonlinear thermoelectrics using the quantum dot in a nanowire, particularly V_{th} and I_{th} as a function of ΔT (see Eq. V.2 and Eq. IV.2). This might help illuminate what parameters can affect the nonlinear behavior.

In this chapter, nonlinear thermoelectric behavior is studied. The thermovoltage and thermocurrent as a function of ΔT are measured at low temperatures. To observe nonlinear thermovoltage, the heating current (I_H) is applied at the source contact. At zero bias, the thermovoltage as a function of ΔT is measured at various gate voltages (see Section III.3.2). The experimental results exhibit the nonlinear behavior as a

function of ΔT which includes, as an extreme example, even a complete sign reversal of thermovoltage. To help in understanding the experimental results, the Landauer equation is used to calculate thermocurrent in the presence of energy-dependent transmission functions.

Thermoelectrics has two driving forces, namely voltage and temperature differences. In the following, first the linear-to-nonlinear IV relation is reviewed. Then the non-linear thermoelectrics analog of the IV relation is discussed, namely a thermovoltage driven by temperature gradient.

The linear relation of current and voltage is described by the conductance, $G = V/I$. This relation can be derived from the Landauer equation for electric current, Eq. II.13. At low temperatures, $T \to 0$, the Fermi function at the source and drain contacts can be approximated as $f_{S,D} \approx \Theta(E - \mu_{S,D})$. When τ is independent of voltage and approximately constant over the range where the transport occurs, this equation becomes

$$
\begin{aligned}
I &= \frac{2e}{h} \int_{\mu_D}^{\mu_S} \tau(E) dE \\
&= \frac{2e}{h} \tau_0 (\mu_S - \mu_D) \\
&= \frac{2e^2}{h} \tau_0 V,
\end{aligned}
\tag{V.1}
$$

where τ_0 is the value of τ in this limit of integration. Hence the current is proportional to voltage, with the proportionality constant being the conductance, which in this case is $(2e^2/h)\tau_0$. For small bias, τ can be considered as voltage independent. However, a

sufficiently large bias will create an electric field inside the device which can change the device potential and thus its transmission function. In general, however, one cannot assume that τ is independent of voltage nor that it is independent of energy, and therefore it should be written as $\tau(E, V)$. Technically, thus, at zero temperature there is no linear response regime, because any energy or voltage dependence of τ will lead to some nonlinear behavior. At finite temperatures, however, these conditions can be relaxed somewhat, because normally thermal smearing will mask any nonlinear effects as long as $eV \ll kT$. The nonlinear effects in voltage can be easily observed in mesoscopic devices since a small voltage drop over a short length can create a sizable electric field which can effect τ. For example, at $T = 1\text{K}$, the thermal energy is 0.086 meV, therefore the bias voltage of 86 μV or greater implies the possibility to observe nonlinear effects.

In the linear response regime, the thermovoltage can be related to the temperature gradient via the Seebeck coefficient, $V_{th} = S\Delta T$. In the nonlinear regime, thermovoltage can be written as an expansion in the temperature gradient:

$$V_{th} = S_1\Delta T + S_2(\Delta T)^2 + S_3(\Delta T)^3 + \cdots , \tag{V.2}$$

where S_i is the Seebeck coefficient of the ith-order term. For small $\Delta T/T$, the first-order term dominates. But as ΔT becomes larger the higher-order terms will start to compete with the linear term as shown in the following sections.

The investigation of thermoelectrics in low-dimensional systems has so far largely focused on the linear regime where $\Delta T \ll T$. The lack of attention in nonlinear

behavior from the mesoscopic research community is in part due to a lack of suitable platform and in part to a challenge of thermometry. The first, and maybe only, experiment that reported observing strongly nonlinear thermoelectrics was done by Staring et. al. [50] where they observed a sign reversal in thermovoltage of a quantum dot in 2DEG as a function of a heating current. However, no theoretical explanation was offered.

To observe a strong nonlinear effect, the device must have sharp, non-monotonic energy features. This is another limitation which many mesoscopic systems do not possess. For example, a quantum point contact has been predicted to show only a weakly nonlinear effect due to the monotonic transmission function [51] and has been confirmed experimentally [52, 53].

With the thermometry technique developed in our lab which allows carrying out thermoelectric experiments and temperature measurements simultaneously, the quantum dots in nanowires provide the well-suited platform for nonlinear thermoelectric experiments. In addition, the transmission function of quantum dots is equipped with the delta-like function which is a requirement for observing strongly nonlinear behavior [54].

Experimental Results

Using the heating technique described in Section III.2, a temperature gradient is established. At a particular gate voltage, the thermovoltage and thermocurrent are

measured as the heating current is varied. The thermometry technique described in
Chapter IV is then used to convert from heating current to temperature gradient.
Figure 5.1(b) shows an example of thermovoltage as a function of ΔT at different
gate voltages. These gate voltages were selected because they show various degrees
of nonlinear behavior. These examples exhibit a linear behavior for a small $\Delta T/T$
(dashed lines in Fig. 5.1(b)).
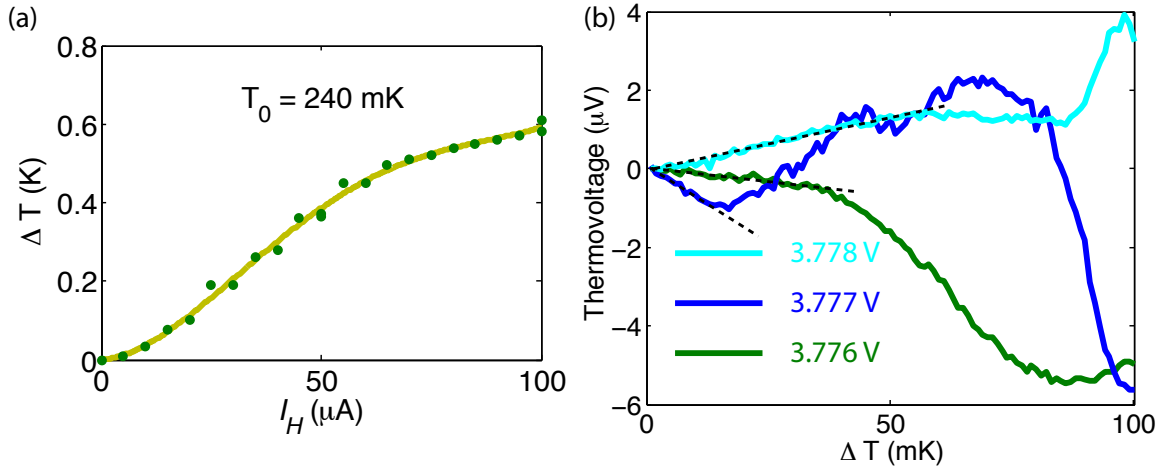
Figure 5.1. (a) The temperature calibration curve used in conversion from I_H to
ΔT. The full dots are the data obtained using the technique discussed in Chapter IV
and the solid line is the fourth-order fitting curve. (b) Thermovoltage is measured as
a function of the heating current. Then using the calibration curve in (a), V_{th} as a
function of ΔT is obtained. The dashed lines indicate where V_{th} behaves linearly.

The goal is to make a model for a strong nonlinear behavior. In the following, the
thermocurrent is used instead of thermovoltage. This is because in thermocurrent
measurements, the voltage is constant which makes the use of Landauer modeling
much easier. In the experiment, the bias voltage is set such that only μ_H (μ_C) is
in the vicinity of the dot's transmission resonance while μ_C (μ_H) is kept further

away from the resonance (see Fig. 5.2(a)). This will allow the omission of cold (hot) side contribution to thermocurrent in the modeling. Here the operating point is a combination of gate and bias voltages such as the green circle in Fig 5.2(a). For each operating point, the thermocurrent is measured as the ac heating current is varied. See Section III.3.1 for details of the thermocurrent measurement.

Figure 5.2(c) shows the nonlinear thermocurrent data measured at $V_G = 3.105$ V and various bias voltages. The thermocurrents shown here were selected because they display extreme nonlinear behavior. In all three data sets, there is apparently no linear regime. Each curve starts out with a parabolic behavior. Similarly, in the modeling section, the linear regime is also limited to very small ΔT. For -2.9 mV bias data, the thermocurrent displays strongly nonlinear behavior. At ΔT about 100 mK ($\Delta T/T \approx 0.18$), a sign reversal of I_{th} is observed.

Modeling Thermocurrent

The goal of this section is to illuminate the cause of nonlinearity using the Landauer approach. First the transmission function for the particular quantum dot is found based on an IV measurement. Then using this transmission function, I_{th} is calculated from the Landauer formalism. Though this model works quite well for weak nonlinear thermocurrent, it cannot produce the sign reversal observed in experiments. A 'fake' transmission function is used in order to see whether one can predict conditions where one would observe a sign reversal. This model takes into account an energy
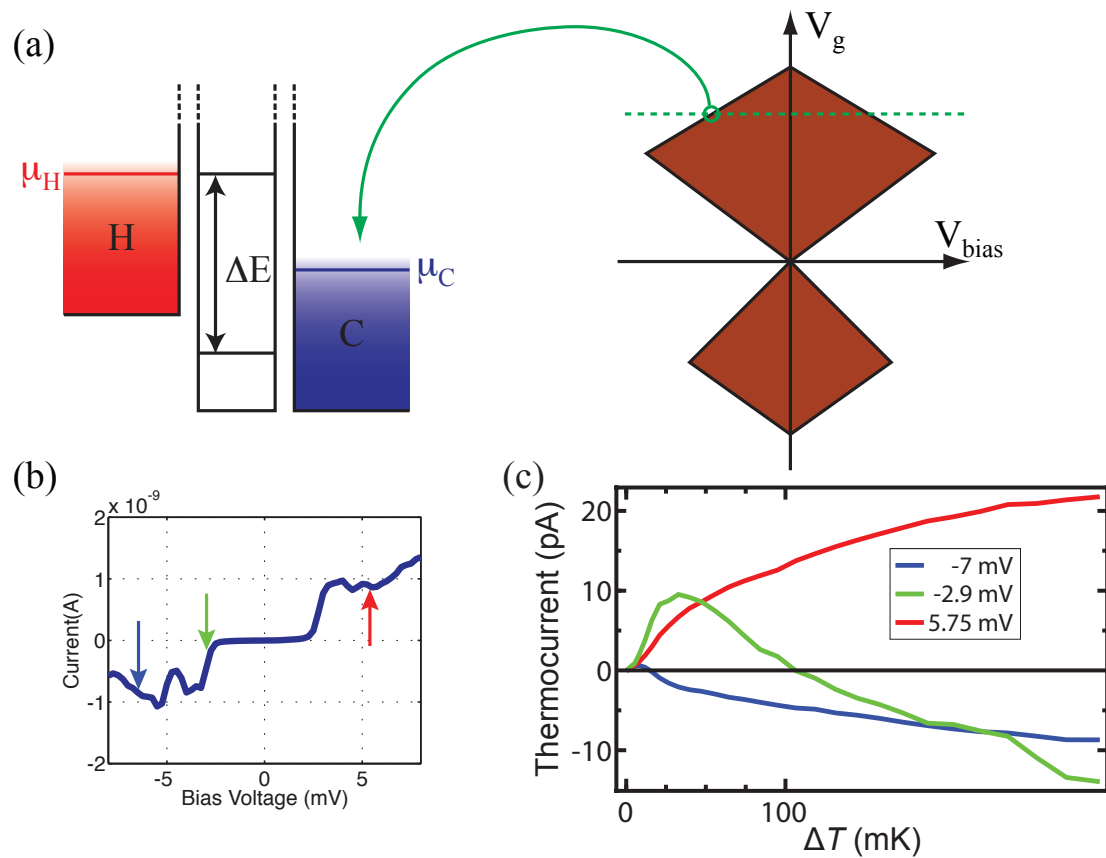
Figure 5.2. (a) The energy diagram of the quantum dot as function of bias and gate voltages. In this configuration, the cold reservoir contribution to the thermocurrent can be ignored. The circle on the right figure indicates a point that corresponds to the configuration shown in the diagram on the left where the diagram on the left is located. The diagram on the left corresponds to the green arrow in (b) where μ_H line up with μ. (b) The IV measurement at gate voltage of 3.5 V. The arrows indicate the operating point for each measurement. (c) The thermocurrent as a function of temperature difference for each bias voltage in (b). Each color corresponds to the applied bias in (b) indicated by the arrow. At -2.9 mV bias, the thermocurrent exhibits sign reversal at $\Delta T \approx 100$ mK. The cryostat temperature is 550 mK.

dependence $\tau(E)$ but assumes no voltage dependence $\tau(V)$. Indeed the simulation is able to produce a sign reversal but at a much higher $\Delta T/T$ than observed in the experiments. We will therefore discuss other factors that might play a role in the observed nonlinear thermoelectric behavior.

The Landauer equation in full form for the current is

$$I = -\frac{2e}{h} \int [f_H(\mu_H, T_H) - f_C(\mu_C, T_C)]\tau(E)dE, \tag{V.3}$$

where the voltage is assumed to drop symmetrically on both ends, $\mu_{H,C} = \mu \pm eV/2$. As mentioned in the experiment section, the bias voltage is applied such that only μ_H (μ_C) is relevant (see Fig. 5.2(a)). As a result, the Fermi function of the cold (hot) side can be dropped from the equation. The lock-in amplifier measures the rms amplitude of the ac thermocurrent as it oscillates between the maxinum (at full ΔT) and minimum (at $\Delta T = 0$) value. Therefore, for negative bias where only μ_H is close to the resonant level, the thermocurrent can be written as

$$\begin{aligned}
I_{th} &= I(\Delta T_H) - I(\Delta T_H = 0) \\
&= -\frac{2e}{h} \int [f_H(\mu_H, T + \Delta T_H) - f_H(\mu_H, T)]\tau(E)dE \\
&= -\frac{2e}{h} \int \mathcal{F}(E)\tau(E)dE, \tag{V.4}
\end{aligned}$$

where $\mathcal{F}(E) = f_H(\mu_H, T + \Delta T_H) - f_H(\mu_H, T)$.

In comparison to the measured data, the model needs the actual transmission function for this particular quantum dot, which is not a priori known. The transmission function is obtained by converting an IV measurement and using Eq. V.1. The

differential conductance is defined as $G = dI/dV$ and τ can be written as

$$\tau \approx \frac{G}{2e^2/h}. \tag{V.5}$$

This approximation assumes the near absolute zero temperature. The IV data are measured at sub-Kelvin range ($T = 550$ mK) which should give an acceptable result.

The IV data in Fig. 5.3(a) is measured at 550 mK cryostat temperature with 3.105 mV gate voltage which is the same condition used in the thermocurrent measurement. Then the IV data is interpolated to create a better resolution in modeling. The numerical differentiation of current over voltage, $\Delta I/\Delta V$, gives the differential conduct-ance. The transmission function is obtained by dividing the differential conductance with the unit of quantization, $2e^2/h$, as explained above and displayed in Fig. 5.3(b). To verify its validity, the obtained τ is inserted into Eq. II.13 to calculate the current as a function of bias voltage and then is compared to the resulting current in the IV data. Figure 5.3(a) shows that the numerical result (red dashed line) using the transmission function described above (green line in Fig. 5.3(b)) agrees with the measured data (blue dots). This means that τ obtained in this method is a good approximation of the real transmission function.

Using this transmission function, the expected thermocurrent as a function of ΔT_H (Eq. V.4) is calculated for comparison with the measured data. For a strong nonlinear thermocurrent, such as the data recorded at -4.25 mV bias voltage (dashed blue curve in Fig. 5.4(b)), the model manages to give a similar trend only for small ΔT. For weakly nonlinear regime such as the data from -5 mV bias voltage, as
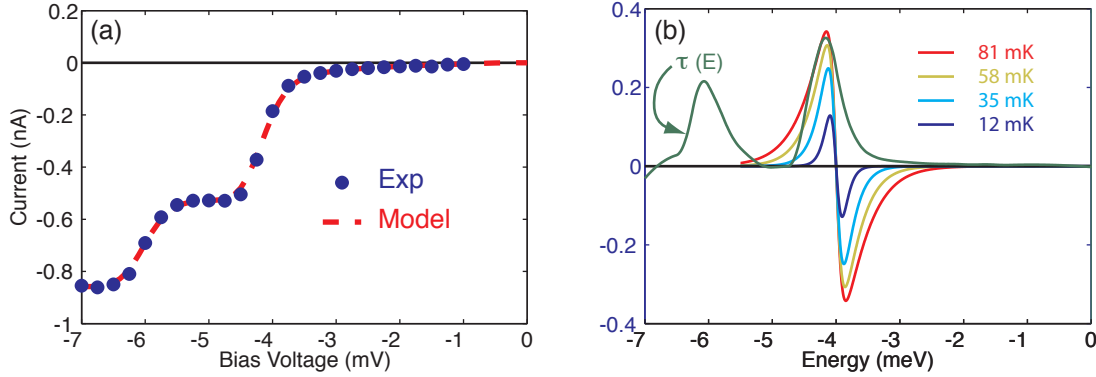
Figure 5.3. (a) IV measurement at the same V_{gate} where thermocurrents are measured (3.105 V) and the model using τ from eq. V.5. (b) A plot of $\mathcal{F}(E)$ at different ΔT: 12 (blue), 35 (cyan), 58 (gold), 81 mK (red). The zero crossing of $\mathcal{F}$ indicates the operating point on τ. This plot shows that as ΔT increases, more electrons (positive portion of $\mathcal{F}(E)$) can transmit to the cold side while the holes (negative portion of $\mathcal{F}(E)$) are blocked by the vanishing transmission function.

shown in Fig. 5.4(b), the modeling produces qualitatively an agreement with the experimental data for a larger ΔT range compared to the data from -4.25 mV.

To understand the modeling results, the function $\mathcal{F}$ at various ΔTs is plotted on top of $\tau(E)$ as shown in Fig. 5.3(b). The positive portion of $\mathcal{F}$ represents electron transport while the negative portion represents hole transport. This explains why the thermocurrent gets larger (more negative because the thermocurrent flows in the opposite direction of the temperature gradient) as the temperature increases. For small ΔT, electrons and holes can explore a narrow region around the operating point (-4 mV bias, in this case) where τ is comparable for electrons (the left side of the operating point) and holes (the right side). The resulting thermocurrent is small because electrons and holes can transmit with nearly equal transmission probability.
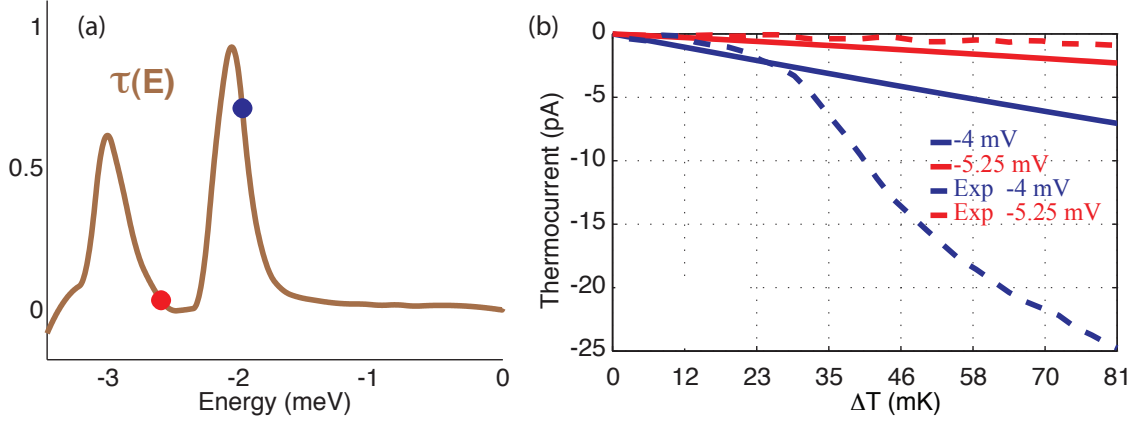
Figure 5.4. (a) The transmission function obtained from the experimental data in Fig. 5.3(a) and two operating points where the data were collected. (b) The experimental (dashed lines) and numrical (solid lines) thermocurrents at two operating points. At -5 mV bias, the model can duplicate the experiment to a certain degree. However, at -4.25 mV bias where the strong nonlinear effect is observed, the model failed to predict the experiment.

As the temperature increases, this window expands allowing more electrons and holes to contribute. However only electrons will benefit from this expanding window because the transmission function is large where $\mathcal{F}$ is positive and almost zero where $\mathcal{F}$ is negative. Hence thermocurrent becomes larger as ΔT increases. This explains the linear behavior of the experimental data. However, it cannot explain the larger nonlinear increase observed in data at -4 mV.

In an attempt to simulate the sign reversal as observed in measured thermocurrent, the thermocurrent was calculated from the Landauer equation using an artificial Lorentz transmission function (see Eq. II.12 and Fig. 5.5). Here the cryostat temperature is taken to be 2 K and ΔT range from 0 to 6 K. Hence $\Delta T/T$ ranges from 0

to 3. When the operating point is off the resonance (the green dot in Fig. 5.5(b)), the nonlinear thermocurrent is observed. This again can be explained by the role of τ and $\mathcal{F}$. The thermocurrent is a result of the competition between the electrons (positive $\mathcal{F}$) and holes (negative $\mathcal{F}$). For small ΔT, electrons and holes contributions to thermocurrent are comparable. As ΔT becomes larger, more holes can transmit via the adjacent peak while the electron contribution is saturated as there is no more channel for transmission. As ΔT increases, the thermocurrent gets smaller and eventually changes its sign. For the operating point in the middle of the trough, only a weakly nonlinear behavior is observed. Now holes flow via the right peak (τ) while electrons flow via the left peak which has a higher magnitude. This leads to increased thermocurrent as ΔT increases. To observe the sign reversal, this model requires a larger ratio of $\Delta T/T$ ($\sim$ 2.2) than observed in the experiment. From comparing these two operating points, it is clear that asymmetry in transmission function plays a significant role in the nonlinearity of the thermocurrent.

Nonlinear thermoelectrics is investigated by using the Landauer approach and comparing these results with the experiment. Many factors contribute to the nonlinear behavior such as the competition between the electrons and holes transports. Also the placement of the position of the operating point (bias and gate voltages) does play some role in this nonlinear behavior.

The modeling with τ referred from IV measurement has mixed success. The model is in agreement with weak nonlinear data (Fig. 5.4(b)) but is unable to predict
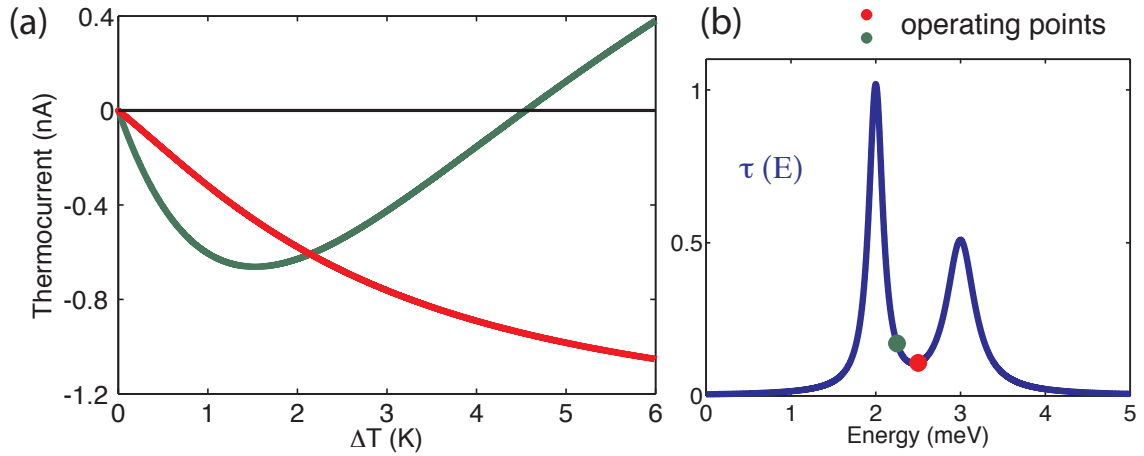
Figure 5.5. (a) Thermocurrent calculated from the artificial Lorentzian transmission function in (b), see Eq. II.12. This extreme example shows that the model does predict nonlinearity in ΔT. (b) The artificial transmission function generated from Lorentzian function. The two peaks are 1 meV apart and T is 2 K. The asymmetry of transmission function plays a role in nonlinear thermocurrent.

the result for strongly nonlinear data. The artificial Lorentzian transmission function is able to reproduce a sign reversal but at higher $\Delta T/T$ than observed in experiments. One of the possible reasons that the model only predicts the nonlinear effect at the comparable ratio of $\Delta T/T$ is that the model assumes the energy dependence transmission function $\tau(E)$. However, τ obtained from the IV measurement may contain voltage dependence. A better way to determine the energy dependence transmission function is needed in order to improve the agreement between the experiment and modeling.

CHAPTER VI

THERMOVOLTAGE LINESHAPE OF QUANTUM DOTS

<u>Introduction</u>

One of strategies to enhance the figure of merit ZT is to increase the thermopower, S. The ability to predict the operating conditions where the system reaches the maximum value of S is therefore important to the thermoelectric performance. Thermovoltage is induced by a temperature difference across a thermoelectric material and is related to thermopower via $V_{th} = S\Delta T$ at zero current condition. As a function of gate voltage, V_{th} and S have the same lineshape. Quantum dots have been shown to exhibit different thermovoltage lineshapes. Staring $et\ al.$ had observed a sawtooth-shaped lineshape in an experiment where $kT \approx 0.065\Delta E$ [50]. This behavior was also predicted by Beenakker and Staring [55]. Their theory assumed first-order tunneling, so called sequential tunneling, with $\Gamma \ll kT, \Delta E$. In doing so, they neglected any virtual tunneling processes and a finite width of the transmission function. Later on, Dzurak $et\ al.$ observed a lineshape more similar to the derivative of conductance peaks, as one would expected from the Mott relation [56]. However, in this case the quantum dot had a ten times larger energy spacing, $\Delta E \approx 167kT$, compared to Staring $et\ al.$ Also the magnitude of the thermovoltage from these reports was quite different. On

the theoretical side, Turek and Matveev [57] showed that the difference between the two lineshapes could be explained by the contribution of sequential tunneling and cotunneling which depend on temperature.

Here it is shown that the difference in lineshape of the thermovoltage can be predicted simply from the knowledge of the energy spacing, ΔE, and the transmission width with respect to thermal energy, Γ/kT, regardless of the tunneling processes involved. The experimental data was measured by Ann I. Persson. The numerical calculation was done by the author.

<u>Experiments and Modeling Results</u>

To observe different thermovoltage lineshapes experimentally, one needs the ability to vary the transmission width, Γ, and energy spacing, ΔE in quantum dots. This can be achieved by varying the thickness and the distance between the two barriers on the nanowire (see Fig. 3.1). Instead of producing various quantum dot samples, two QD samples with a large difference in Γ and ΔE were fabricated. Then Γ/kT and $\Delta E/kT$ were varied by changing the cryostat temperature. Sample number 1 (QD1) is made from InAs/InP heterostructure nanowire with $InAs_{0.8}P_{0.2}$ as the dot material. For sample number 2 (QD2) InAs is used as the dot material. The inset of Fig. 6.1(d) shows a SEM image of the heterostructure nanowire which contains QD2 sample (which cannot be seen at this magnification). The fabrication process for a quantum dot defined by the double barrier structure is discussed in Chapter III.
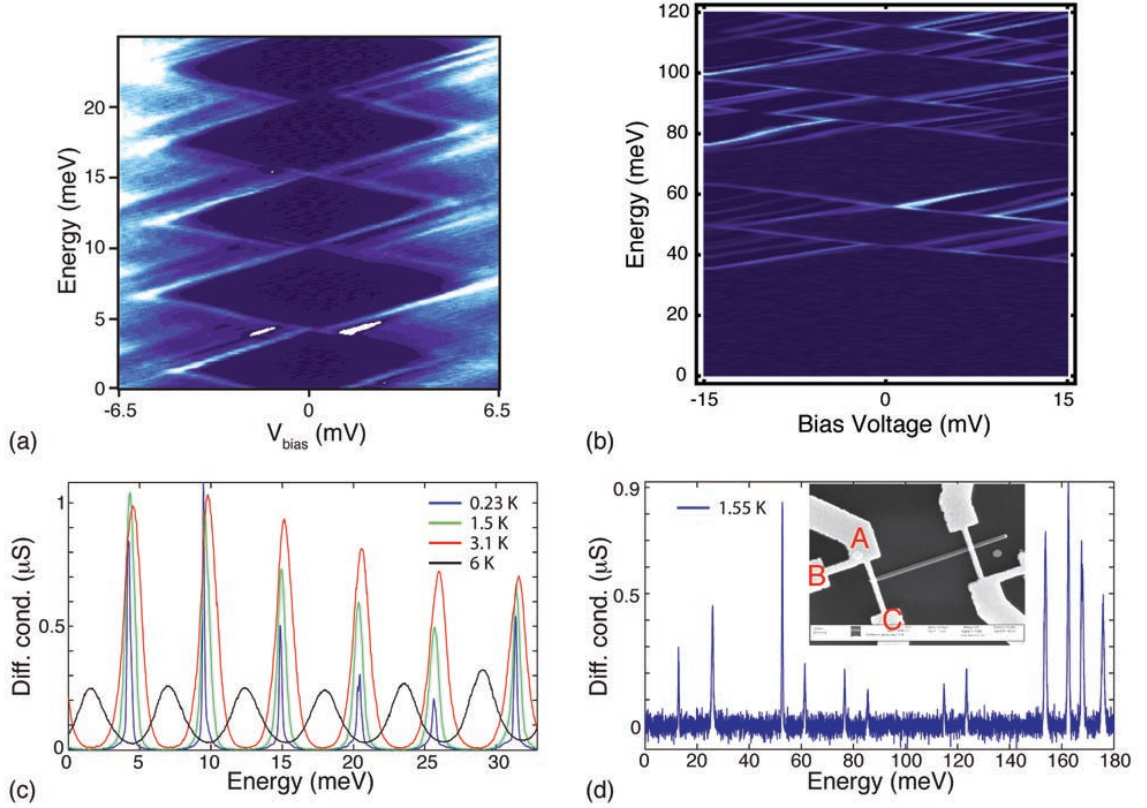
Figure 6.1. (a)-(b) Coulomb diamond of the differential conductance for QD1 and QD2, respectively. (c) The conductance measurements of QD1 showing the equally spaced resonance peaks (5.3 meV) due to the fact that charging energy (E_C) is larger than quantized energy (δE). (d) The differential conductance of QD2 showing the characteristic conductance peaks where quantized energy and charging energy are comparable. Figures courtesy of Dr. Ann Persson, Ref. [58].

Figures 6.1 (a)-(b) show Coulomb blockade diamonds for the differential conductance of QD1 and QD2, respectively. The conversion factors, obtained from the CB diamond, for QD1 and QD2 are $\alpha = 0.3133$ eV/V and 0.06 eV/V, respectively. These factors are used to convert the gate voltage in experiments into the energy scale. The thermovoltage measurement is already discussed in Section III.3.2. and the heating method is covered in Section III.2.2.

The transmission function is again extracted from an IV measurement as previously discussed in Section V.3. For QD1, $\Gamma \approx 160$ μeV which is equivalent to a temperature of 1.8 K. As for QD2, $\Gamma > 30$ μeV. Here the quantization energy is larger than the charging energy $E_C = 8.7$ meV. This is why the first few conductance peaks exist in pairs (see Fig. 6.1(d)).

At each cryostat temperature T, increasing the heating current, I_H, increases the peak of thermopower, as shown in Fig. 6.2. As T increases, making Γ/kT smaller, the lineshapes evolve from the derivative-like to the sawtooth, in agreement with modeling results Fig. 6.5.

Figures 6.3 and 6.4 show the measured thermopower and simulations for QD1 and QD2, respectively. The simulations are based on the τ deduced from IV measurement under the isothermal conditions, and represent a prediction of the thermovoltage based on knowledge of the conductance peaks alone. For QD1, qualitatively the modeling produces results about the same magnitude. The data for QD2 shows an asymmetry in lineshape for the left resonance which is not captured by this model.

The modeling of the thermovoltage has been discussed in Section II.3. In the simulations, a sawtooth-shaped lineshape is observed when $\Gamma/kT < 10^{-6}$ as shown in Fig. 6.5(a). For a delta transmission function $\tau(E) = \delta(E - E_0)$, if μ does not coincide with E_0, the system will adjust itself by changing V_{th} until the system reaches the equilibrium condition where $\Delta f = 0$ at the resonance energy, as shown in Fig. 6.6. If μ is located away from the resonance energy, the thermovoltage needs to increase for
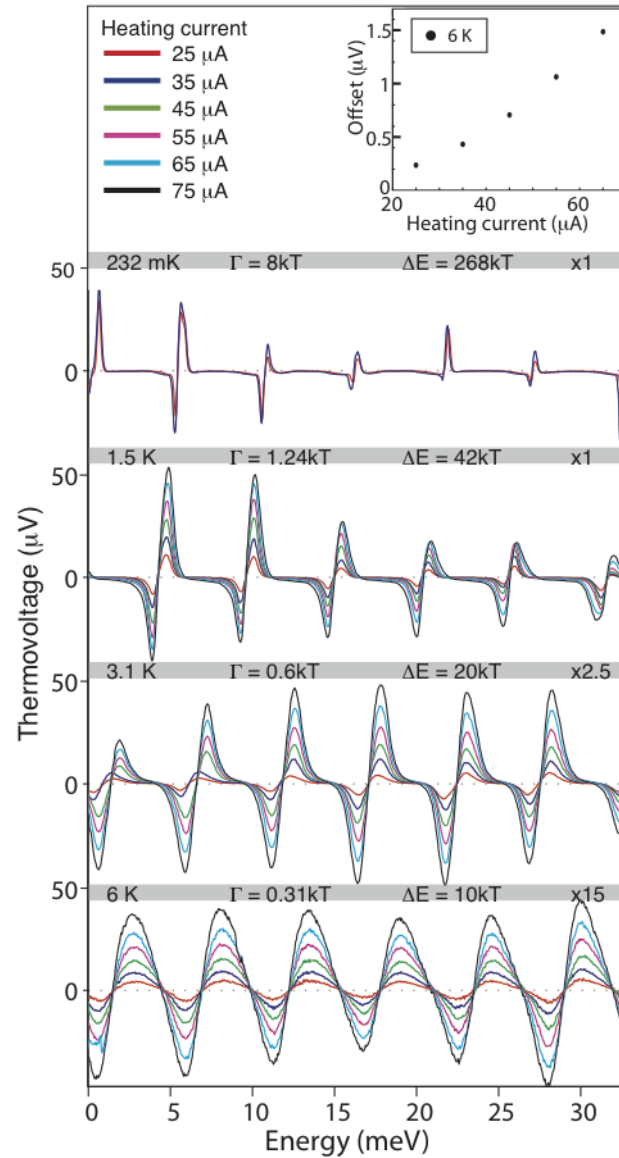
Figure 6.2. Thermovoltage of QD1 for different cryostat temperature T and various heating currents. The first three cryostat temperatures show the measured thermovoltages. For 6 K cryostat temperature, the offset has been added to center the curves at $V_{th} = 0$. The magnitude of the offset for each heating current is shown in the inset. At $T = 3.1$ K and 6 K, the thermovoltage signals are multiplied by a factor (shown at the gray bar) for easy comparison. Figure courtesy of Dr. Ann Persson, Ref. [58].
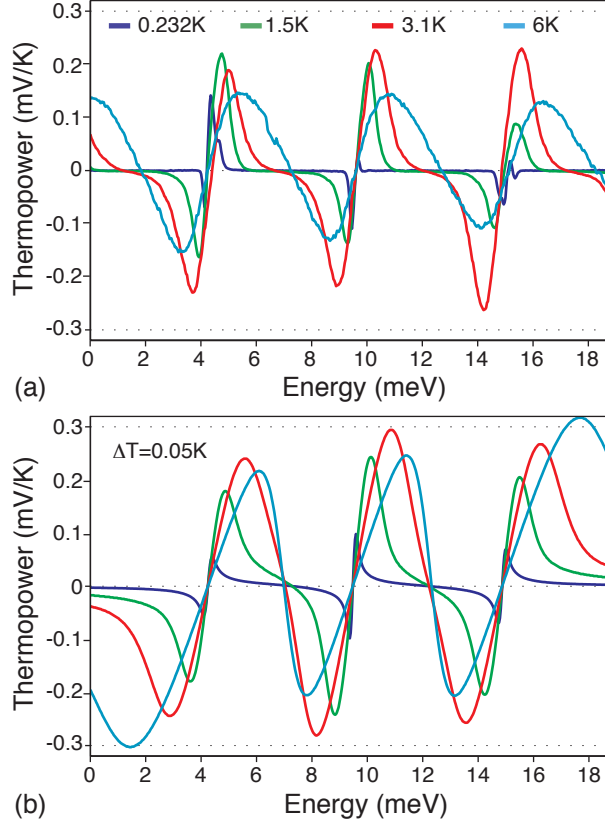
Figure 6.3. (a) Thermopower, S, as a function of energy for QD1, using the measured thermovoltage and an estimated ΔT at $T = 0.232$ K (blue), 1.5 K (green), 3.1 K (red), and 6 K (cyan). (b) The simulations of thermopower at the same T with $\Delta T = 50$ mK and using $\tau(E)$ extracted from conductance measurements.

$\Delta f = 0$ to occur. The thermovoltage will keep increasing until μ is half way between the first and second resonance. At that point, the thermovoltage switches its sign. In contrast, when the transmission function has a finite width, the thermovoltage will reach its maximum value, depending on the value of Γ/kT, and then goes down to zero (see Fig. 6.5(a)). The reason is the transmission function is not zero everywhere like in the delta transmission but has a very insignificant value. The difference between the two lineshapes occurs when μ is many kT away from the resonance energy. Thus
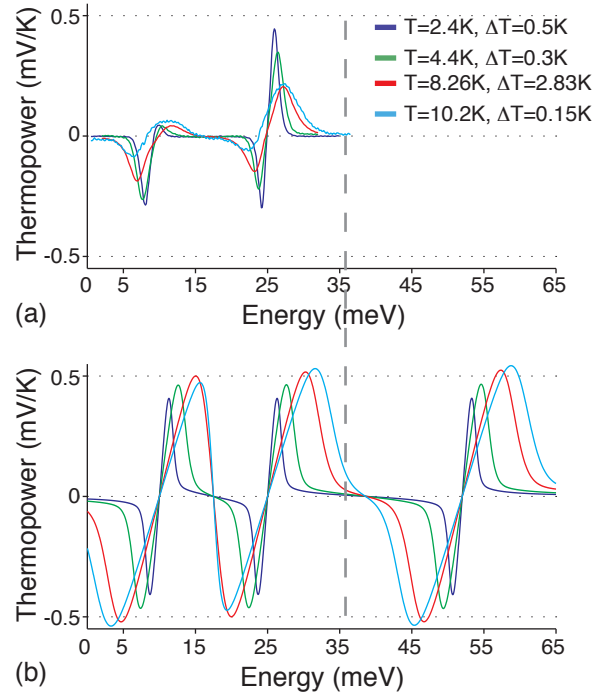
Figure 6.4. (a) Experimental thermopower data for QD2 as a function of energy for $T = 2.4$ K, 4.4 K, 8.26 K, and 10.2 K. ΔT obtains from the technique describe in Chapter IV. (b) The simulations of thermopower at the same T and ΔT as in (a).

the convolution between Δf and τ at this location could produces the zero current condition without increasing V_{th}.

The effect of ΔE on V_{th} is shown in Fig. 6.5(b). It shows that when the energy spacing is less than $25kT$, the thermovoltage peak is lower than the maximum value because the adjacent resonance energy begins to contribute to the thermovoltage with opposite sign.

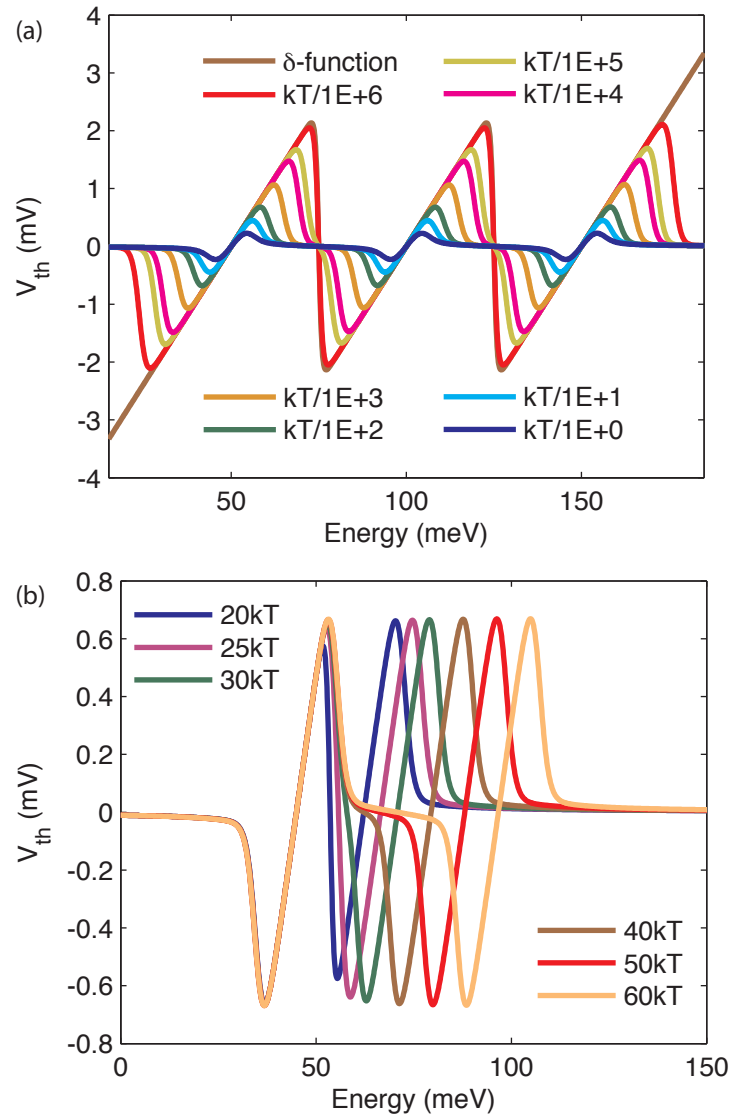**Figure 6.5.** (a) A modeling result showing the effect of the finite width transmission function for $T = 10$ K, $\Delta T = 1$ K, and $\Delta E = 50$ meV $\sim 58kT$. Narrow transmission widths ($\Gamma/kT \to 0$) yield a sawtooth lineshape while the broader width has a derivative-like lineshape. (b) Thermovoltage as a function of energy with varying ΔE for $T = 10$ K, $\Delta T = 1$ K, and $\Gamma = kT/100$.
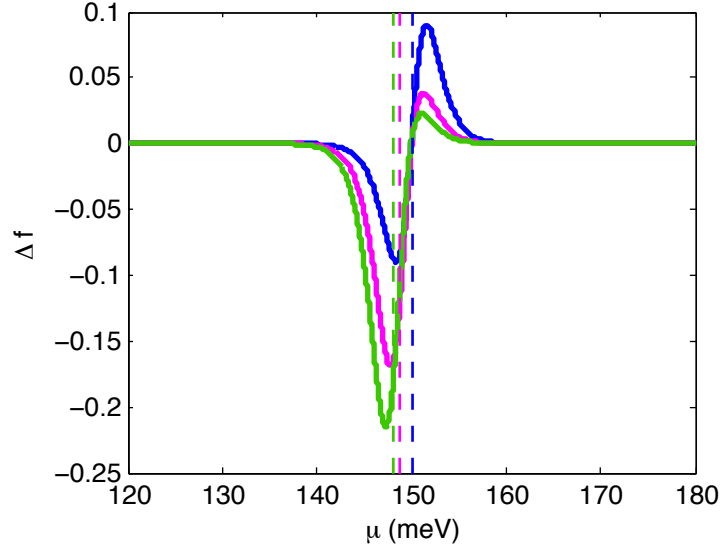
Figure 6.6. Plot of $\Delta f = f_H - f_C$ for $\mu = 148.1$ meV (green), 148.8 meV (magenta), and 150 meV (blue) where $E_0 = 150$ meV. $T_C = 10$ K and $T_H = 15$ K. The dashed lines indicate where μ is located for each case.

Conclusions

Thermovoltage is an important parameter for achieving high figure of merit. Maximizing its value will significantly boost ZT, as V_{th} is related to S and has the same lineshape. The results here indicate that to achieve this goal requires: i) narrow transmission width compared to thermal energy ($\Gamma/kT \rightarrow 0$) and ii) the resonance peaks have to be surprisingly well separated ($\Delta E \approx 25kT$). In this work, it is also shown that the lineshape can be inferred from the transmission width and the energy spacing, and no detailed knowledge of the mechanism contributing to lineshape broadening needs to be known.

CHAPTER VII

EFFICIENCY AND POWER PRODUCTION COMPARISON OF

LOW-DIMENSIONAL SYSTEMS

Introduction

It is a well known fact that any heat engine operating at Carnot efficiency is unable to deliver useful power. Thus it has no real use in practical applications. A more practical performance indicator of a heat engine would be a measure of the trade-off between efficiency and power production. Low-dimensional systems are good candidates for improving efficiency via increasing the figure of merit ZT. Thus it is reasonable to investigate among low-dimensional systems which system is suitable for high efficiency at high power output. Low-dimensional systems that are currently under investigation for energy conversion applications, including quantum dot superlattices [12], molecular junction [49], thin film superlattices [13, 59], carbon nanotubes [60], and heterostructure thermionic devices [61]. The goal here is to consider the idealized case for each fundamental low-dimensional electron system.

In this chapter, the thermoelectric performances of three low-dimensional systems is modeled and compared. These performances are efficiency, power, and efficiency at maximum power (η_{maxP}). These low-dimensional systems are a quantum dot (QD), a

one-dimensional (1D) ballistic conductor, such as a quantum point contact or an ideal

nanowire, and a thermionic (TI) power generator, which is a thin film semiconductor

embedded into a bulk semiconductor with a lower band gap. Figure 7.1 illustrates

a 1D channel and a TI device and their corresponding energy diagrams (for QD see

Fig. 2.1).

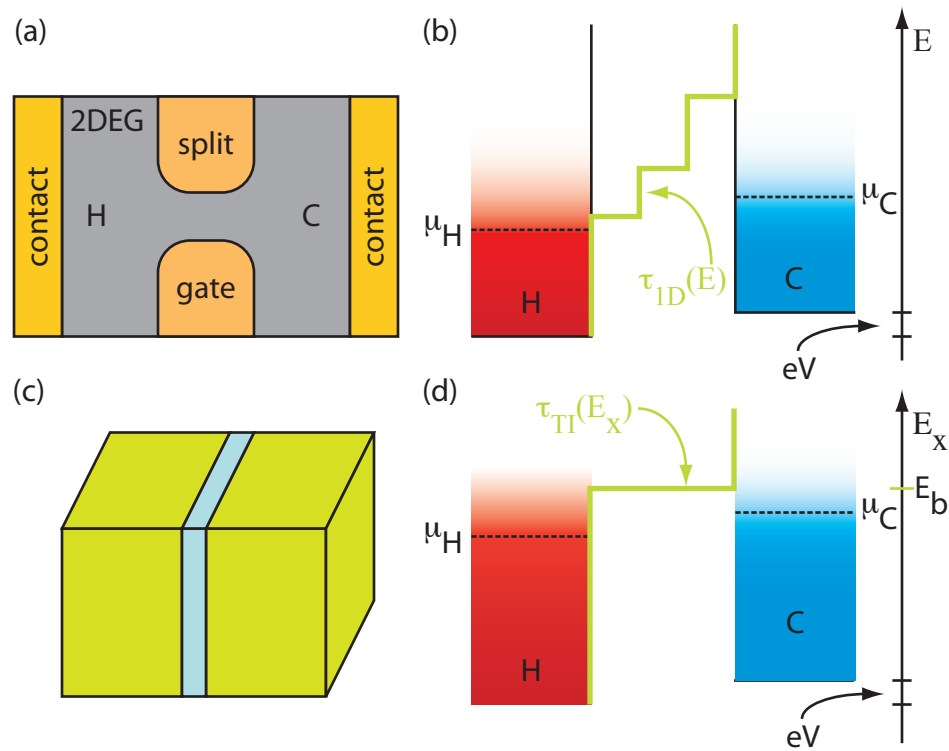**Figure 7.1.** Cartoons illustrate device schematics and energy diagrams of a 1D conductor (a)-(b) and a thermionic power generator (c)-(d).

For quantum dots and nanowires, the Landauer approach is employed to calculate

the relevant thermoelectric properties. For the thermionic systems, the Tsu-Esaki

equation is used [28, 62].

Heat is carried by two types of carriers, namely electrons/holes and phonons. Here

the phonon contribution will be excluded from the analysis, because understanding the electronic properties is the main focus of this study. As a result, the overall efficiency will be less than what will be presented here. The phonon contribution can be added by evaluating the parasitic heat flow. Also these systems are assumed to obey ballistic transport (the devices size is smaller than the elastic and inelastic scattering length of the charge carriers) and we assume $\Delta T \ll T, eV \ll kT$.

To compare the performances of these systems, the power production and heat flux out of the hot side are calculated as a function of bias voltage V and chemical potential μ (see Section II.3). Then the maximum power, maximum efficiency and efficiency at maximum power for each system are identified for comparison.

Models and Simulation Data

Quantum dots have already been discussed in the previous chapter, so only 1D and TI will be briefly reviewed.

A One-Dimensional Conductor

A ballistic one-dimensional conductor is a system that has spatial confinement along the transverse direction and the length is shorter or comparable to the electron mean free path. This short length ensures the ballistic transport. An example of 1D conductors is a quantum point contact [63, 64]. Also nanowires [15, 16, 33, 37] can be ballistic if the length is kept quite short.

In an ideal 1D system, the confinement potential is described by a hard wall

potential while inside the channel the confinement potential is zero. The electron energy in the channel can then be written as

$$E(x, y, z) = E_n(y, z) + \left(\frac{\hbar^2 k^2}{2m^*}\right), \tag{VII.1}$$

where n is an integer number that indicates the subband and m^* is the electron effective mass (see Fig. 7.2(a)).

The transmission function for the ideal 1D system can be written as

$$\tau(E) = \sum_{n=1}^{\infty} \Theta(E - E_n).$$

where Θ is the Heaviside step function (see Fig. 7.2(b)). Using this transmission function in the Landauer equation, thermoelectric quantities can be derived in the same way as described in Chapter II for QD systems.

A Thermionic System

Figure 7.1(c) shows a thermionic system which is a single thin-film energy barrier embedded into bulk semiconductors with a lower band gap. The barrier edge energy E_b in Fig. 7.1(d) is defined as $E_b = (\hbar k'_x)^2 / 2m^*$ where k'_x is the barrier-edge wave vector and m^* is the effective mass. The thin-film barrier filters electrons' cross-plane momentum, denoted by k_x, such that electrons with $k_x < k'_x$ will be blocked. This holds true even if the total electron energy is larger than the barrier edge energy $E > E_b$. During the transport, the lateral momentum is assumed to be conserved.

A thermionic system was first proposed to be used as a refrigerator via evaporative mechanisms where hot electrons are selectively emitted over single/multiple barrier(s)
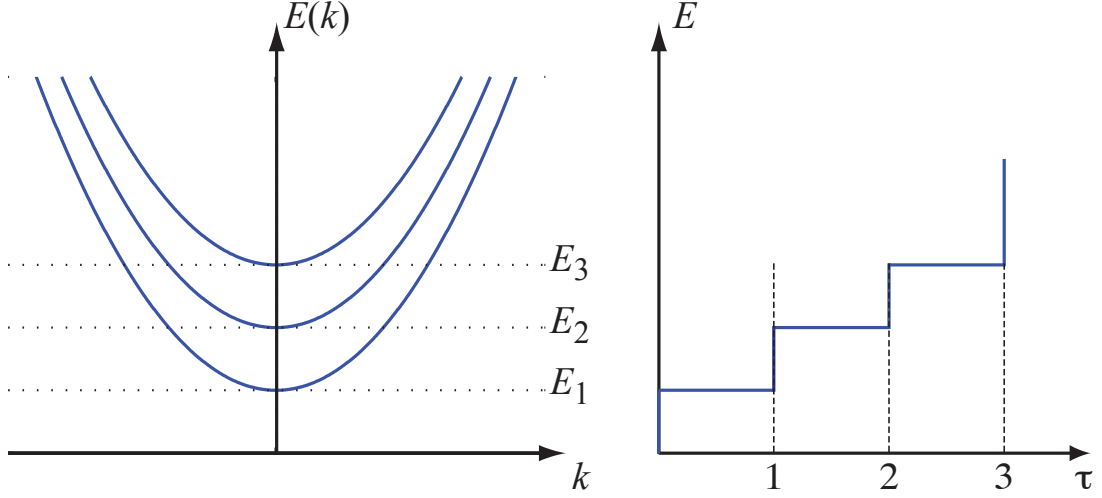
Figure 7.2. (a) The dispersion relation of electrons in a 1D channel. The parabolic relation between wave vector k in x-direction and energy E of the conduction electrons. The quantized energy of the y- and z- directions $(E_n(y,z))$ is the bottom of the parabolic curve. (b) The corresponding transmission function $\tau(E)$. Each step of τ corresponds to the bottom of each subband in (a).

[65, 66]. In this study, electron tunneling is neglected. This can be achieved by using a relatively thick barrier (larger than tunneling length but smaller than elastic relaxation length).

Tsu-Esaki Formula

This approach was first derived to calculate the tunneling current through a superlattice such as the resonant tunneling diode (RTD) device [28, 62]. It is also applicable to a TI device. Since the tunneling is excluded in TI, the only way electrons can transmit is over the barrier edge, E_b. Hence the transmission function for TI is a single step function, $\tau_{TI}(E_x) = \Theta(E_x - E_b)$ where $E_x = (\hbar k_x)^2/(2m^*)$, see Fig. 7.1d.

The current density [28] can be written as

$$J_e = \frac{2e}{(2\pi)^3 \hbar} \int_0^\infty dE_x \int_0^\infty k_t dk_t \int_0^{2\pi} d\phi [f_l(E_x, k_t) - f_r(E_x, k_t)] \tau(E_x) \qquad \text{(VII.2)}$$

where k_t is the wave vector in the transverse direction. The Fermi function on the left and right sides are

$$f_{l/r} = \left[1 + \exp\left(\frac{E_x + E_t - \mu_{l/r}}{kT_{l/r}} \right) \right]^{-1}.$$

Let the left and right sides correspond to the hot and cold reservoirs, respectively. The angular integration gives 2π. Using a change of variable from momentum space to energy space, $E_t = (\hbar k_t)/2m^*$, the current density becomes

$$J_e = \frac{m^* e}{2\pi^2 \hbar^3} \int [\zeta_H - \zeta_C] \tau(E_x) dE_x, \qquad \text{(VII.3)}$$

where

$$\zeta_{H/C} = kT_{H/C} \log\left[1 + \exp\left(-\frac{E_x - \mu_{H/C}}{kT_{H/C}} \right) \right].$$

And the power density is written as $\mathcal{P} = V J_e$.

The heat flux per unit area out of the hot side, $\dot{q}_H$, can be calculated in a similar way using heat instead of electric charge. It is given by

$$\dot{q}_H = \frac{m^*}{2\pi^2 \hbar^3} \int [\epsilon_H \zeta_H - \epsilon_C \zeta_C] \tau(E_x) dE_x, \qquad \text{(VII.4)}$$

where $\epsilon_{H/C} = E_z + kT_{H/C} - \mu_H$. Note that the energy of the lateral direction is averaging to the thermal energy, $kT_{H/C}$, of the originating reservoir. This is due to the fact that the in-plane momentum can take on any value.

Simulation Data

Figures 7.3 - 7.5 show power (power density in the case of the TI system) and efficiency normalized to the Carnot value as a function of μ and V. The red curve represents the open-circuit voltage. A pocket, defined by the zero-voltage line and the open-circuit voltage, is the region where the devices operate as a heat engine that produces electric power. The green line passes through the location of maximum power. In each case the maximum efficiency occurs close to the open-circuit voltage line while the maximum power is located near the band edge (resonant peak in QD case) and at intermediate V. Note that in the 1D and TI cases, the power (power density) falls off quickly below the first subband.

In comparing thermoelectric performances of these systems, care must be taken with units of thermoelectric quantities such as power and heat flux. For example, QD and 1D systems create a certain amount of power per mode (or per device) while a TI system produces power per area (power density). One possible approach, which is utilized here, is to convert the current density and heat flux per unit area of TI into current and heat flux, which are the quantities produced by QD and 1D systems. Thus the power production of TI systems is obtained from

$$P_{TI} = A_0 \mathcal{P}_{TI},$$

where A_0 is the effective area of the TI device. Essentially the current (power) and heat flux for the same cross-sectional area of nanowire are being compared to these systems and the value of A_0 used here is 100 nm^2.
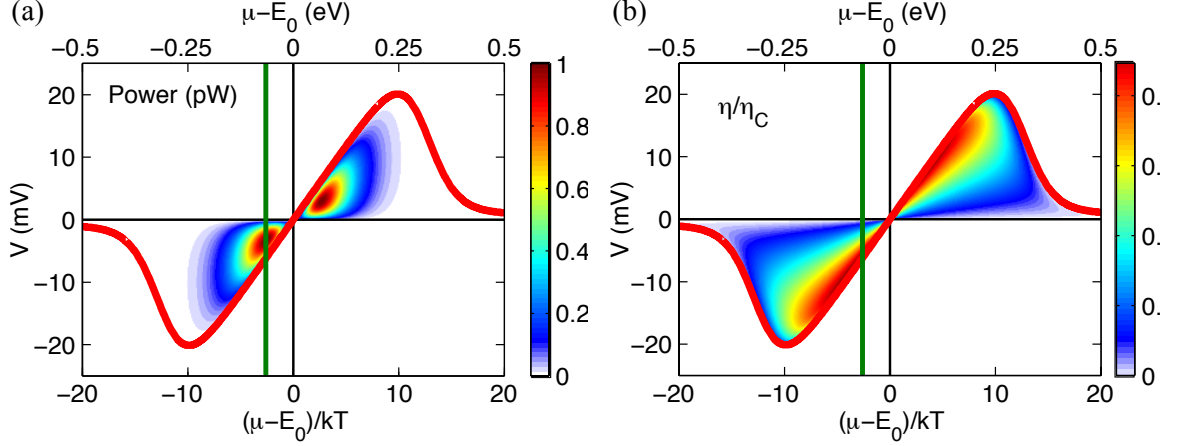
Figure 7.3. Simulation data for quantum dots. (a) Power (in pW) and (b) normalized efficiency of a quantum dot with $\Gamma = 0.01kT$ and $T_C = 300$ K and $T_H = 330$ K. The green line indicates the μ that yields maximum power.
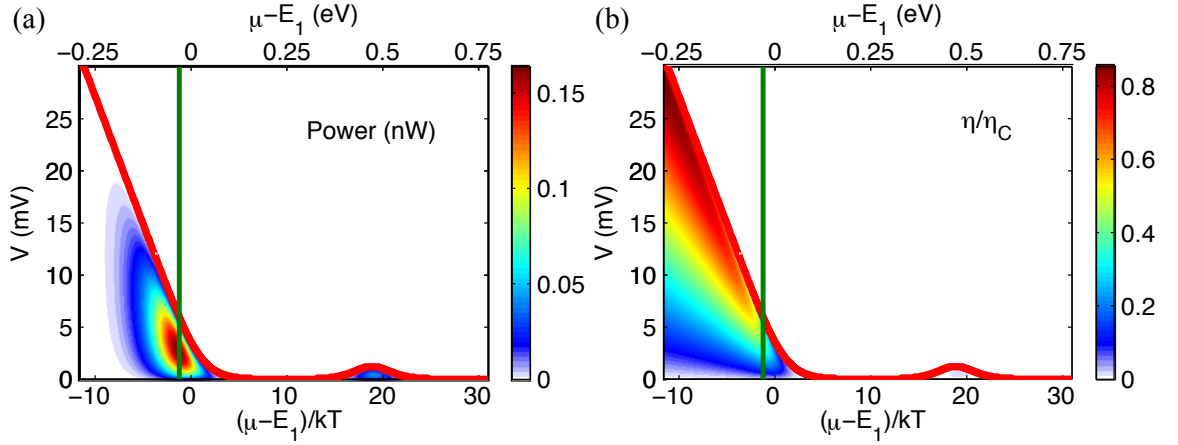

Figure 7.4. Simulation data for 1D conductors. (a) Power (in nW) and (b) normalized efficiency of the nanowire with $T_C = 300$ K and $T_H = 330$ K. The green line indicates the μ that yields maximum power.
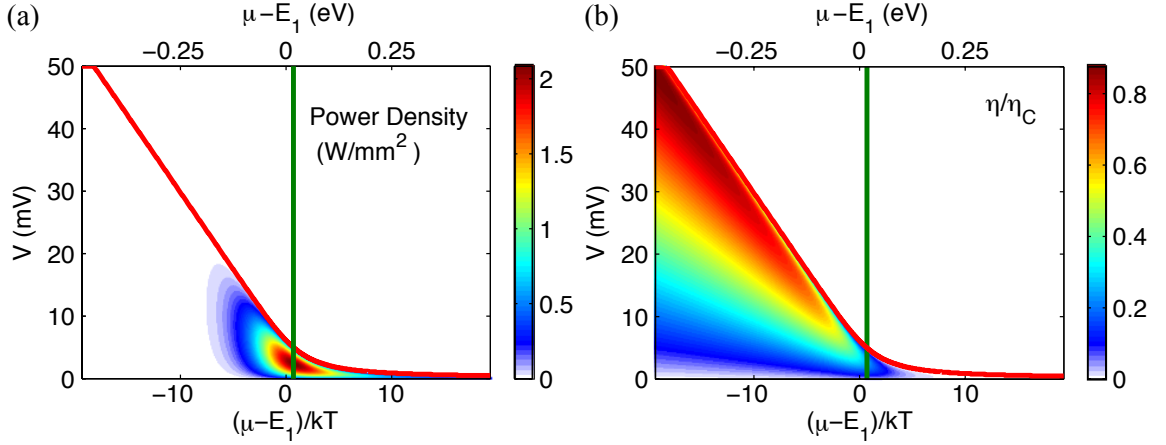
Figure 7.5. Simulation data for TI systems. (a) Power density (in W/mm^2) and (b) normalized efficiency of thermionic generator with $T_C = 300$ K and $T_H = 330$ K. The green line indicates the μ that yields maximum power.

Results and Discussions

The thermoelectric performance in terms of maximum power P_{max} and efficiency at maximum power η_{maxP} will be compared to determine which of the three systems considered here provides the best trade-off performance. One way to display thermo-electric performance is to pair power and normalized efficiency for each operating point (μ, V) and to then plot these pairs along a line of constant μ. This gives a 'loop'. All loops for all μ fill up a region in $(\eta/\eta_C, P)$ space as shown for QD systems in Fig. 7.6. The performance of quantum dots depends on the width of the transmission function (Γ). In this figure, the narrow width yields a high efficiency but an infinitesimal power. To get more power from quantum dots, the transmission width must be broadened, which unavoidably diminishes the efficiency as explained below. At around $\Gamma \approx 2.25kT$, the power reaches its maximum value while the

efficiency drops to 17% of the Carnot efficiency (see Fig 7.7). Further increasing the width yields low efficiency and low power.
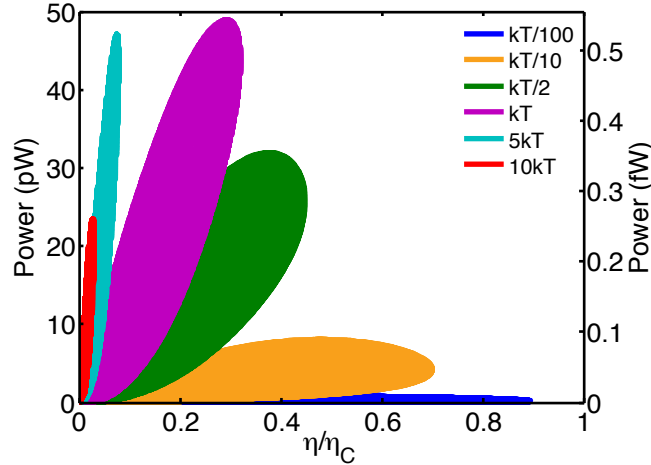

Figure 7.6. Plot of normalized efficiency vs. power for quantum dots with various transmission width. $T_C = 300$ K and $T_H = 330$ K. For each Γ, the whole plane in Fig. 7.3 is scanned.

Carnot efficiency occurs when a single, sharp energy level coincides with E_0 (Eq. I.13). This occurs when the Fermi function of the hot contact at this particular energy equals that of the cold contact. For a transmission function with finite width (Eq. II.12), electrons can probe a small range of energy around the resonant peak. In general, this allows the current to flow in either directions. If more electrons flow from the hot side to the cold side than the opposite direction, the net thermal-driven current will be larger and so is the power output. However, as electrons with energy higher than the chemical potential can transmit, the heat flow also increases. When the power gain cannot compensate for the heat loss, efficiency suffers. And when Γ
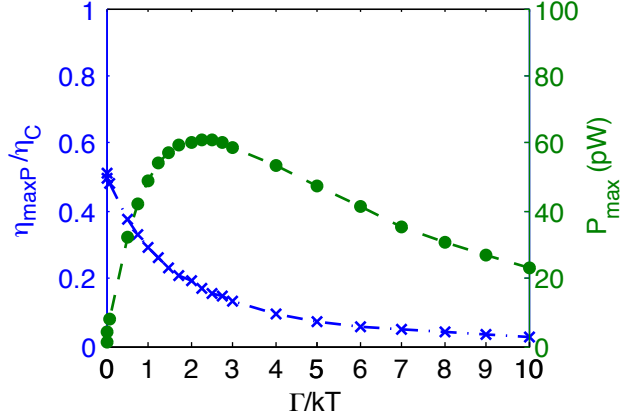
Figure 7.7. η_{maxP} (blue, crosses) normalized by Carnot efficiency, and maximum power (green, full dots) of a quantum dot as a function of Γ/kT for $T_C = 300$ K and $T_H = 330$ K. Maximum power peaks around $\Gamma/kT = 2.25$. Efficiency at maximum power η_{maxP} approaches $\eta_{CA} = 51\%$ for small Γ.

is about $2.25kT$ or larger, the current becomes saturated as there are no particles available to participate because the energy range where $\Delta f \neq 0$ is covered by τ (see Fig. 7.8). Further increasing the width will only attenuate the current because the contribution from the parasitic back-flow current starts to dominate.

For 1D systems, the thermoelectric performance is better for the first subband compared to the second subband as shown in Fig. 7.4. The reason is that at an appropriate (μ, V), the current can be tuned to flow only from hot to cold if only the first subband is occupied. In contrast, at subbands other than the first, there will always be the current flowing from the cold side to the hot side, reducing the net current, see Fig. 7.9. Thus the performance of 1D systems in the following comparison will be referred to that of the first subband.
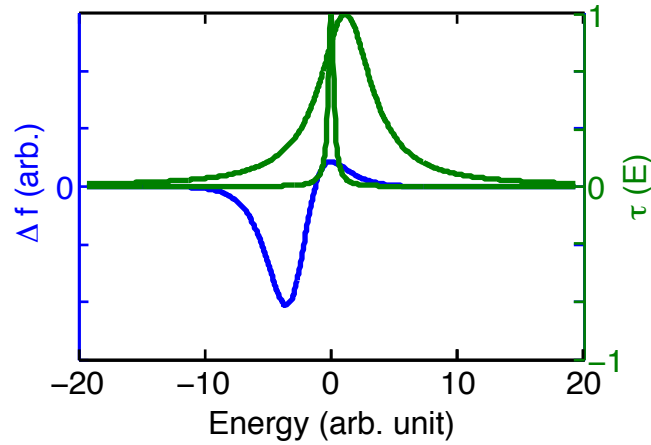
Figure 7.8. The transmission functions with different widths (green) and the difference in Fermi function of the hot and cold sides, $\Delta f = f_h - f_c$ (blue), using μ and V that result is maximum power. The resonance peaks are plotted in the approximate position where maximum power would be achieved. The positive Δf means electrons flow from the hot to the cold reservoirs. The convolution of the two quantities affects the thermal-driven current. This shows that the broader width ($\Gamma > 2.25kT$) suppresses the current and power.
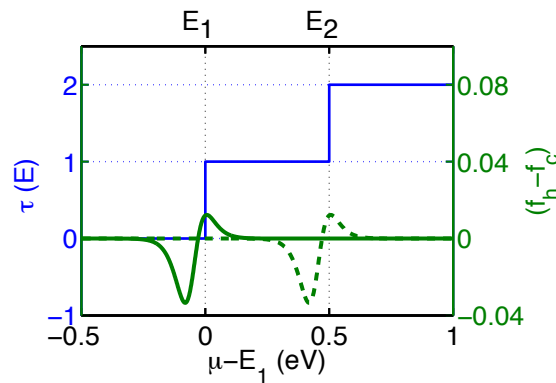
Figure 7.9. The 1D transmission function (blue) and the two different Δf (green). The positive portion of Δf means electrons flow from hot to cold. In the solid green line, $\mu_{H/C}$ locates just below the bottom of the first subband while in the dashed green line, it locates below the second subband. In the former case, electrons flow only from hot to cold because below the first subband $\tau = 0$. In the latter case, electrons flow in both directions and the net current suffers from electrons flow from cold to hot.

Maximum Power

The modeling results show that the maximum power is proportional to T^2 for QD (at fixed Γ) and 1D, and to T^3 for TI. The power as a function of temperature is shown in Fig. 7.10. For temperature below cross-over temperature $(T_\times)$, the temperature where power production of 1D equals that of TI, 1D has the highest maximum power while above this temperature TI is more productive, with moderate η_{maxP}, than the others. Quantum dot is the least productive in terms of power, even with the highest maximum power $(\Gamma \approx 2.25kT)$.
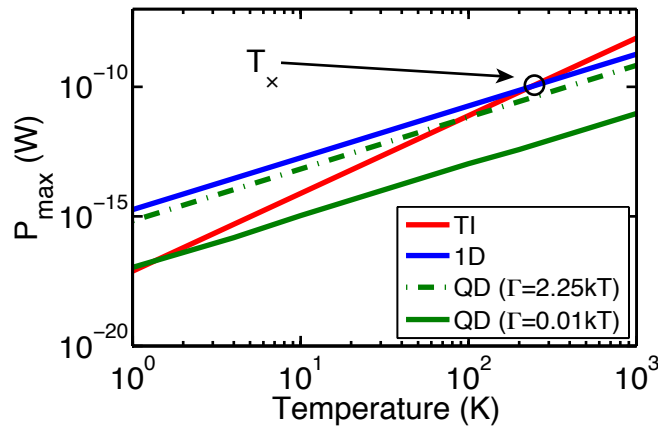
Figure 7.10. Maximum power as a function of temperature for $m^* = 0.07m_e$ with $\Delta T/T = 0.1$. $T_\times$ is the temperature where 1D and TI systems yield the same power. $T_\times$ depends on the cross-sectional area and on the electron effective mass.

Whether 1D or TI system produces the highest power, depends on the operating temperature compared to the cross-over temperature $T_\times$. This performance is valid as long as all the assumptions are met. One might be able to change which system outperforms the other by adjusting the cross-over temperature. This temperature

depends on the effective mass of TI material and the cross-sectional area of 1D device used in conversion of TI's power density as shown in Fig. 7.11. Increasing m^* results in higher power in TI which lower $T_\times$. Larger A_0 means smaller power density in 1D system which also lower $T_\times$.
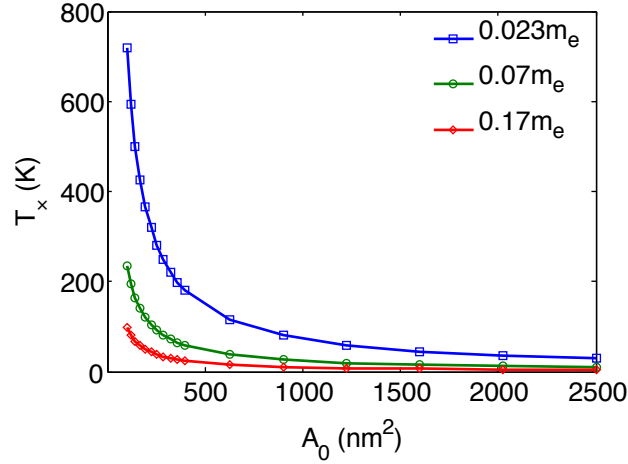
Figure 7.11. $T_\times$ as defined in Fig. 7.10 as a function of effective area A_0 of a 1D system for different effective mass: InAs $(0.023m_e)$, GaAs $(0.07m_e)$, and PbTe $(0.17m_e)$.

Efficiency at Maximum Power

In the seminal work [20], Curzon and Ahlborn had investigated the efficiency at maximum power of Carnot engine and found that the upper limit of this quantity is approximately one-half of Carnot efficiency. Recent works extend this theory by showing that the approximation is universally applied to many systems and an agreement is up to the quadratic term [21, 22, 67, 68]. The Curzon-Ahlborn efficiency is given by

$$\eta_{CA} = \frac{\eta_C}{2} + \frac{\eta_C^2}{8} + \dots \tag{VII.5}$$

Figure 7.12 shows $(\eta/\eta_C, P)$ loops for QD (with $\Gamma = 0.01kT$ and kT), 1D, and

TI at $T =$100, 200, and 300 K. The efficiency at maximum power in each case is

independent of temperature. η_{maxP}/η_C of QD with narrow Γ $(0.01kT)$ is approaching

the Curzon-Ahlborn limit ($\sim 51\%$ of the Carnot efficiency). And η_{maxP} for the other

is below the CA limit. These values are 17%, 36%, and 24% for QD with $\Gamma = 2.25kT$,

1D and TI, respectively.
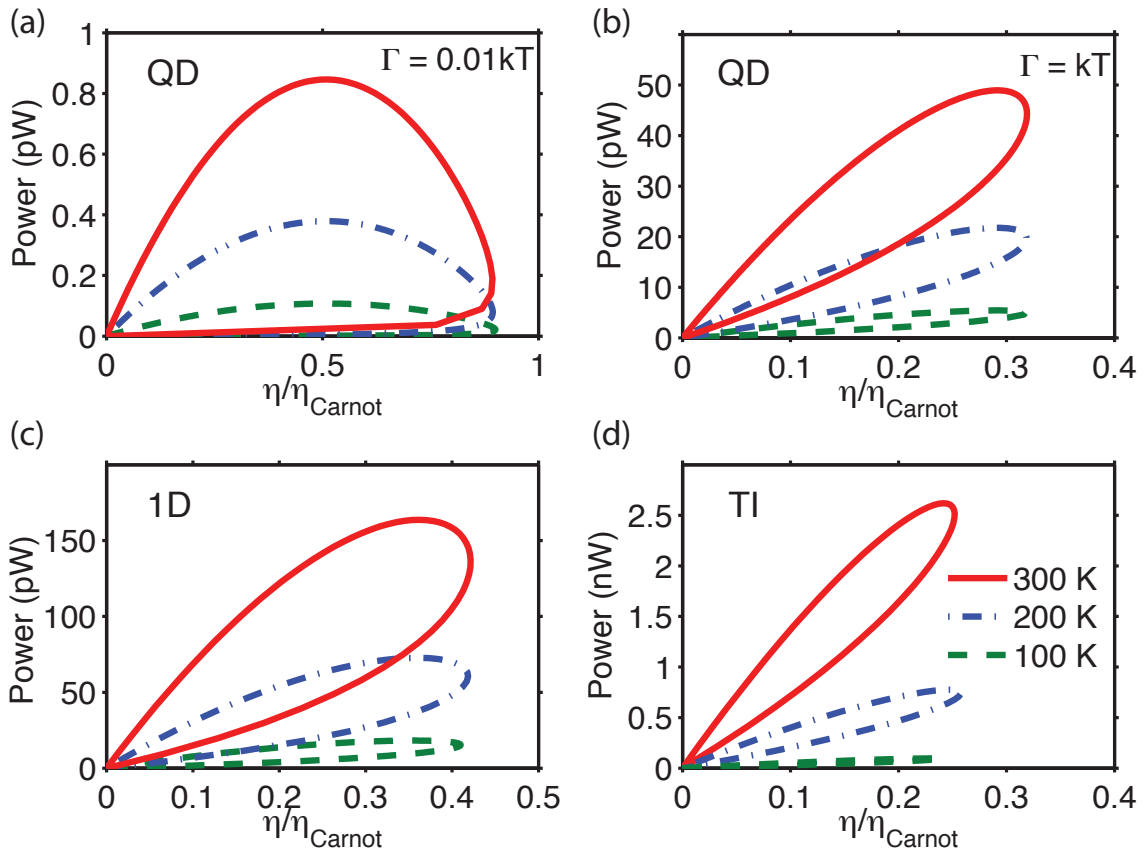

Figure 7.12. (a)-(d) Loops along constant μ chosen at P_{max} of each system (i.e. along the green line of Figs. 7.3(b), 7.4(b), and 7.5(b)) show that efficiency at maximum power is independent of temperature. Note that the power values of the TI system depend on A_0 (see main text), whereas the efficiency values are independent of this choice. The QD's values depend on Γ

Relation to the Thermoelectric Figure of Merit

Here these results are put into the context of traditional thermoelectric figure of merit, Z (see Eq. I.7). And only the electronic contribution is considered, denoted by $(ZT)_{el}$. The actual ZT will be smaller than what is presented here.

$$
\begin{aligned}
ZT &= \frac{S^2 \sigma T}{\kappa_e + \kappa_l} \\
&= \frac{S^2 \sigma T}{\kappa_e (1 + \kappa_l / \kappa_e)} \\
&= (ZT)_{el} \left(\frac{1}{1 + \kappa_l / \kappa_e} \right)
\end{aligned}
\tag{VII.6}
$$

Ioffe [69] derived the thermoelectric efficiency as a function of ZT. The efficiency can be written as

$$
\eta = \frac{M - 1}{M + T_C/T_H} \eta_C,
\tag{VII.7}
$$

where $M = \sqrt{1 + ZT}$ and T needs to be taken as the average temperature $(T_H + T_C)/2$.

Here $(ZT)_{el}$ is calculated in order to compare with the maximum efficiency of these systems. First the thermopower is obtained from

$$
S = \left(\frac{V_{oc}}{\Delta T} \right) \Big|_{I=0}
$$

and the ratio of κ_e/σ is calculated from

$$
\frac{\sigma}{\kappa_e} = \frac{G}{K},
\tag{VII.8}
$$

where the conductance G and thermal conductance K are defined as

$$
G = \left(\frac{dI}{dV} \right) \Big|_{\Delta T = 0}
$$

$$
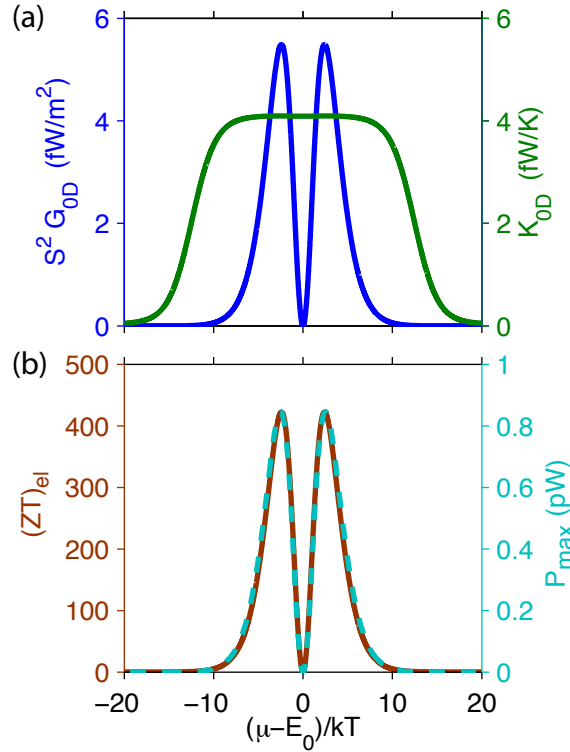K = \left(\frac{\dot{Q}_H}{\Delta T} \right) \Big|_{I=0}.
$$

Figure 7.13. Plot of (a) Power factor (blue) and thermal conductance (green), (b) $(ZT)_{el}$ (brown) and P_{max} (cyan) as a function of $\mu - E_0$ for a quantum dot with $\Gamma = 0.01kT$ and $T_C = 300$ K and $T_H = 330$ K.

Figure 7.13 shows the result of these calculations for quantum dots. $(ZT)_{el}$ is much larger than that observed in the measurements of real systems which is in the order of unity. This is due to the fact that κ_l has been omitted from the consideration. And in semiconductors, usually κ_l is larger than κ_e. Including κ_l would reduce ZT significantly. To compare the modeling results with Eq. VII.7, for each Γ the maximum efficiency and maximum $(ZT)_{el}$ are paired together. Figure 7.14 shows a plot of this pairing and the result agrees with Eq. VII.7.
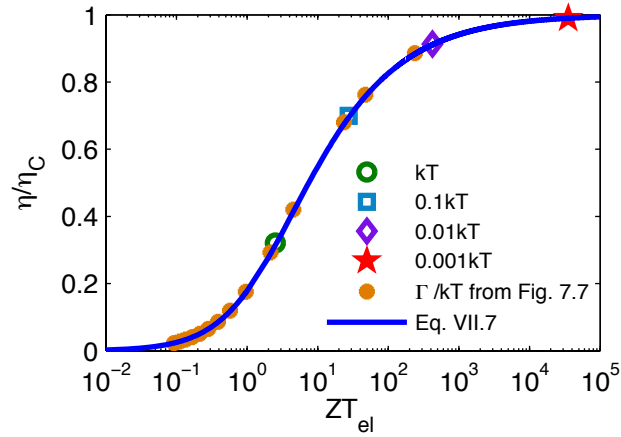
Figure 7.14. Plot of η/η_C vs. ZT_{el} for various Γ. The blue solid line is predicted from Eq. VII.7.

Discussion and Outlook

QDs provide the highest efficiency with the narrow transmission width but offer the very little power production. At the highest maximum power output for QDs ($\Gamma = 2.25kT$), the efficiency has been reduced to 17% of the Carnot efficiency. Below a cross-over temperature, 1Ds have the highest power of the three, at a moderate efficiency at 36% of the Carnot limit (in the same range as those of conventional fluid/gas heat engine, which generally also operate near maximum power).

This comparison can be improved to be meaningful in real devices. Including the lattice (phonon) heat transfer into consideration would provides a better picture of efficiency and the figure of merit. Adding the phonon contribution, the total heat flux out of the hot reservoir is now written as $\dot{Q}_{\text{total}} = \dot{Q}_H + \dot{Q}_l$ where $\dot{Q}_l$ mean the total heat flux due to phonon contributions. Thus the total efficiency become $\eta = \eta_e(\dot{Q}_H/\dot{Q}_{\text{total}})$

where $\eta_e = P/\dot{Q}_H$ is the electronic efficiency. Note that the inclusion of the phonon contribution would favor the lower dimensional system like 1Ds as surface scattering in nanowires strongly suppresses phonon heat conductivity to a value significantly below the bulk value [15, 16, 70–73]. However, power production would not change since it is a result of charge transport only.

CHAPTER VIII

CONCLUSIONS

The (near) Carnot efficiency of particle-exchange heat engine can be attained when only electrons at a particular energy are allowed to flow [18]. This is because the Fermi distributions of the hot and cold reservoirs at this energy are equal and particles flow with no preferred directions. A double-barrier quantum dot provides the energy-selective filtering required for realizing this reversible thermodynamic process. InAs/InP heterostructure nanowires are studied as quantum dot heat engines. This research is part of the goal to measure quantitatively the thermoelectric efficiency of a quantum dot and prove that the quantum dot indeed can operate with near Carnot efficiency.

A quantum dot in a nanowire offers a vast array of thermoelectric applications. Utilizing thermoelectric devices in real situations requires that the subband energy separation has to be larger than room-temperature thermal energy, $\Delta E \gg kT$. This is readily achieved in quantum dots. Furthermore, the quantum dot can be selected to operate as an n-type or a p-type by tuning gate voltage. Thereby quantum dots can be used either as a heat pump or a heat engine.

To measure the electronic efficiency, the temperature difference across the dot has to be established and quantified. This is achieved by using a novel heating and

thermometry techniques where the source/drain contacts for electrical measurement can also be used as a heat source. The thermometry technique measures electron temperature rises on hot and cold sides of the dot. This technique allows an all-in-one experimental device. The quantum-dot thermometry technique presented here offers a useful tool for fundamental physics relating to thermoelectric and thermal transport of a quantum dot. Other properties related to the thermoelectric performance of the quantum dot have also been studied throughout the course of this research. Thermovoltage and thermocurrent have been observed to exhibit a strong nonlinear behavior even at $\Delta T/T$ as small as 0.06. This nonlinear effect can lessen thermoelectric performance of the quantum dot. Though the transmission function plays an important role in the nonlinear behavior as shown in Chapter V, it is not clearly understood. Future research should look into the role of energy and voltage dependence of the transmission function. A novel method to extract information about transmission is clearly needed.

The thermoelectric figure of merit is enhanced by either increasing power factor $S^2\sigma$ or decreasing heat leak or both. Power factor will benefit from a raise in thermopower more than in electron conductivity. The thermovoltage, which related to thermopower via $S = V_{th}/\Delta T$, have been observed in two different lineshapes. The different lineshapes can be explained by the tunneling processes [57]. Here the lineshape can be predicted from the width of transmission function Γ and the energy spacing ΔE.

Another important property in determining thermoelectric performance of a quantum dot is the phonon transport. Many phonon behaviors in 1D wires are not well understood, such as phonon drag and electron-phonon interaction. Phonon experiments are challenging as they are more sensitive to a measurement than electronic experiments. A suspended nanowire [74] offers a possible platform to study the phonon role.

The low-dimensional comparison in Chapter VII offers another way to assess thermoelectric performance. Instead of optimized efficiency, the desire performance is the efficiency at maximum power. The modeling in Chapter VII shows that ZT of quantum dots is extremely large compared to the observed values in real systems. However, the inclusion of lattice (phononic) thermal conductivity would drastically reduce this number. The inclusion of phonon heat leaks could improve the comparison as it yield a more realistic efficiency and efficiency at maximum power. Note that the phonon scattering may work in favor of the lower dimensional system such as QD and 1D.

BIBLIOGRAPHY

[1] T. E. Humphrey and H. Linke, Physica E **29**, 390 (2005).

[2] L. E. Bell, Science **321**, 1457 (2008).

[3] T. C. Harman, M. P. Walsh, B. E. LaForge, and G. W. Turner, J. Electron. Mater. **34**, L19 (2005).

[4] F. J. DiSalvo, Science **285**, 703 (1999).

[5] B. C. Sales, Science **295**, 1248 (2002).

[6] T. M. Tritt, H. Böttner, and L. Chen, MRS Bulletin **33**, 366 (2008).

[7] L. D. Hicks and M. S. Dresselhaus, Phys. Rev. B **47**, 12727 (1993).

[8] L. D. Hicks and M. S. Dresselhaus, Phys. Rev. B **47**, 16631 (1993).

[9] P. Kim, A. Majumdar, and P. L. McEuen, Phys. Rev. Lett. **87**, 215502 (2001).

[10] C. Yu, L. Shi, Z. Yao, D. Li, and A. Majumdar, Nano Letters **5**, 1842 (2005).

[11] T. C. Harman, P. J. Taylor, D. L. Spears, and M. P. Walsh, J. Electron. Mater. **29**, L1 (2000).

[12] T. C. Harman, P. J. Taylor, M. P. Walsh, and B. E. LaForge, Science **297**, 2229 (2002).

[13] R. Venkatasubramanian, E. Siivola, T. Colpitts, and B. O'Quinn, Nature **413**, 597 (2001).

[14] Y.-M. Lin, S. B. Cronin, J. Y. Ying, M. S. Dresselhaus, and J. P. Heremans, Appl. Phys. Lett. **76**, 3944 (2000).

[15] A. I. Boukai, Y. Bunimovich, J. Tahir-Kheli, J.-K. Yu, W. A. Goddard, and J. R. Heath, Nature **451**, 168 (2008).

[16] A. I. Hochbaum, R. Chen, R. D. Delgado, W. Liang, E. C. Garnett, M. Najarian, A. Majumdar, and P. Yang, Nature **451**, 163 (2008).

[17] G. D. Mahan and J. O. Sofo, Proc. Natl. Acad. Sci. **93**, 7436 (1996).

[18] T. E. Humphrey, R. Newbury, R. P. Taylor, and H. Linke, Phys. Rev. Lett. **89**, 116801 (2002).

[19] T. E. Humphrey and H. Linke, Phys. Rev. Lett. **94**, 096601 (2005).

[20] F. L. Curzon and B. Ahlborn, Am. J. Phys. **43**, 22 (1975).

[21] M. Esposito, K. Lindenberg, and C. Van den Broeck, Europhys. Lett. **85**, 60010 (2009).

[22] M. Esposito, K. Lindenberg, and C. Van den Broeck, Phys. Rev. Lett. **102**, 130602 (2009).

[23] M. Esposito, R. Kawai, K. Lindenberg, and C. Van den Broeck, Phys. Rev. E **81**, 041106 (2010).

[24] H. van Houten, C. W. J. Beenakker, and A. A. M. Staring, in *Single Charge Tunneling*, edited by H. Grabert and M. H. Devoret (Plenum, New York, 1992), vol. B294 of *NATO Advanced Studies Institutes*.

[25] R. Hanson, L. P. Kouwenhoven, J. R. Petta, S. Tarucha, and L. M. K. Vandersypen, Rev. Mod. Phys. **79**, 1217 (2007).

[26] R. Landauer, IBM J. Res. Dev. **1**, 223 (1957).

[27] S. Datta, *Electronic Transport in Mesoscopic Systems* (Cambridge University Press, 1995).

[28] D. K. Ferry and S. M. Goodnick, *Transport in Nanostructures* (Cambridge University Press, 1997).

[29] M. T. Björk, C. Thelander, A. E. Hansen, L. E. Jensen, M. W. Larsson, L. R. Wallenberg, and L. Samuelson, Nano Letters **4**, 1621 (2004).

[30] R. S. Wagner and W. C. Ellis, Appl. Phys. Lett. **4**, 89 (1964).

[31] B. J. Ohlsson, M. T. Björk, M. H. Magnusson, K. Deppert, L. Samuelson, and L. R. Wallenberg, Appl. Phys. Lett. **79**, 3335 (2001).

[32] B. J. Ohlsson, M. T. Björk, A. I. Persson, C. Thelander, L. R. Wallenberg, M. H. Magnusson, K. Deppert, and L. Samuelson, Physica E **13**, 1126 (2002).

[33] M. T. Björk, B. J. Ohlsson, T. Sass, A. I. Persson, C. Thelander, M. H. Magnusson, K. Deppert, L. R. Wallenberg, and L. Samuelson, Appl. Phys. Lett. **80**, 1058 (2002).

[34] M. T. Björk, Ph.D. thesis, Lund University (2005).

[35] A. I. Persson, M. W. Larsson, S. Stenström, B. J. Ohlsson, L. Samuelson, and L. R. Wallenberg, Nature Matters **3**, 677 (2004).

[36] K. A. Dick, K. Deppert, T. M. rtensson, B. Mandl, L. Samuelson, and W. Seifert, Nano Letters **5**, 761 (2005).

[37] M. T. Björk, B. J. Ohlsson, C. Thelander, A. I. Persson, K. Deppert, L. R. Wallenberg, and L. Samuelson, Appl. Phys. Lett. **81**, 4458 (2002).

[38] A. Fuhrer, L. E. Fröberg, J. N. Pedersen, M. W. Larsson, A. Wacker, M.-E. Pistol, and L. Samuelson, Nano Letters **7**, 243 (2007).

[39] M. T. Björk, A. Fuhrer, A. E. Hansen, M. W. Larsson, L. E. Fröberg, and L. Samuelson, Phys. Rev. B **72**, 201307 (2005).

[40] E. A. Hoffmann, Ph.D. thesis, University of Oregon (2009).

[41] L. Shi, D. Li, C. Yu, W. Jang, D. Kim, Z. Yao, P. Kim, and A. Majumdar, J. Heat Transfer **125**, 881 (2003).

[42] L. W. Molenkamp, A. A. M. Staring, B. W. Alphenaar, H. van Houten, and C. W. J. Beenakker, Semicond. Sci. Technol. **9**, 903 (1994).

[43] E. A. Hoffmann, N. Nakpathomkun, A. I. Persson, H. Linke, H. A. Nilsson, and L. Samuelson, Appl. Phys. Lett. **91**, 252114 (2007).

[44] E. A. Hoffmann, N. Nakpathomkun, A. I. Persson, H. A. Nilsson, L. Samuelson, and H. Linke, Physica E **40**, 1605 (2008).

[45] E. A. Hoffmann, H. A. Nilsson, J. E. Matthews, N. Nakpathomkun, A. I. Persson, L. Samuelson, and H. Linke, Nano Letters **9**, 779 (2009).

[46] E. A. Hoffmann and H. Linke, J. Low Temp. Phys. **154**, 161 (2009).

[47] M. F. O'Dwyer, T. E. Humphrey, and H. Linke, Nanotechnology **17**, S338 (2006).

[48] M. S. Dresselhaus, G. Chen, M. Y. Tang, R. Yang, H. Lee, D. Wang, Z. Ren, J.-P. Fleurial, and P. Gogna, Adv. Mater. **19**, 1043 (2007).

[49] P. Murphy, S. Mukerjee, and J. Moore, Phys. Rev. B **78**, 161406 (2008).

[50] A. A. M. Staring, L. W. Molenkamp, B. W. Alphenaar, H. van Houten, O. J. A. Bujk, M. A. A. Mabesoone, C. W. J. Beenakker, and C. T. Foxon, Europhys. Lett. **22**, 57 (1993).

[51] M. A. Çipiloğlu, S. Turgut, and M. Tomak, Phys. Status Solidi B **241**, 2575 (2004).

[52] A. S. Dzurak, C. G. Smith, L. Martin-Moreno, M. Pepper, D. A. Ritchie, G. A. C. Jones, and D. G. Hasko, J. Phys.: Condens. Matter **5**, 8055 (1993).

[53] J. T. Nicholls and O. Chiatti, J. Phys.: Condensed Matter **20**, 164210 (2008).

[54] J. Wang, L. Wan, Y. Wei, Y. Xing, and J. Wang, Mod. Phys. Lett. B **20**, 215 (2006).

[55] C. W. J. Beenakker and A. A. M. Staring, Phys. Rev. B **46**, 9667 (1992).

[56] A. S. Dzurak, C. G. Smith, C. H. W. Barnes, M. Pepper, L. Martín-Moreno, C. T. Liang, D. A. Ritchie, and G. A. C. Jones, Phys. Rev. B **55**, R10197 (1997).

[57] M. Turek and K. A. Matveev, Phys. Rev. B **65**, 115332 (2002).

[58] A. I. Persson, E. A. Hoffmann, N. Nakpathomkun, H. Q. Xu, and H. Linke (2010), in preparation.

[59] H. Böttner, G. Chen, and R. Venkatasubramanian, MRS Bulletin **31**, 211 (2006).

[60] J. P. Small, K. M. Perez, and P. Kim, Phys. Rev. Lett. **91**, 256801 (2003).

[61] D. Vashaee and A. Shakouri, J. Appl. Phys. **101**, 053719 (2007).

[62] R. Tsu and L. Esaki, Appl. Phys. Lett. **22**, 562 (1973).

[63] B. J. van Wees, H. van Houten, C. W. J. Beenakker, J. G. Williamson, L. P. Kouwenhoven, D. van der Marel, and C. T. Foxon, Phys. Rev. Lett. **60**, 848 (1988).

[64] D. A. Wharam, T. J. Thornton, R. Newbury, M. Pepper, H. Ahmed, J. E. F. Frost, D. G. Hasko, D. C. Peacock, D. A. Ritchie, and G. A. C. Jones, J. Phys. C: Solid State Phys. **21**, L209 (1988).

[65] G. D. Mahan, J. Appl. Phys. **76**, 4362 (1994).

[66] A. Shakouri and J. E. Bowers, Appl. Phys. Lett. **71**, 1234 (1997).

[67] Z. C. Tu, J. Phys. A: Math. Theor. **41**, 312003 (2008).

[68] B. Rutten, M. Esposito, and B. Cleuren, Phys. Rev. B **80**, 235122 (2009).

[69] A. F. Ioffe, *Semiconductor thermoelements, and Thermoelectric cooling* (Infosearch, 1957).

[70] N. Mingo and D. A. Broido, Phys. Rev. Lett. **93**, 246106 (2004).

[71] N. Mingo, Appl. Phys. Lett. **84**, 2652 (2004).

[72] F. Zhou, J. Szczech, M. T. Pettes, A. L. Moore, S. Jin, and L. Shi, Nano Letters **7**, 1649 (2007).

[73] F. Zhou, A. L. Moore, M. T. Pettes, Y. Lee, J. H. Seol, Q. L. Ye, L. Rabenberg, and L. Shi, J. Phys. D: Appl. Phys. **43**, 025406 (2010).

[74] G.-T. Kim, G. Gu, U. Waizmann, and S. Roth, Appl. Phys. Lett. **80**, 1815 (2002).